Title: Stable Pom1 clusters form a glucose-modulated concentration gradient that regulates mitotic entry

Authors: Corey A.H. Allard, Hannah E. Opalko, and James B. Moseley*

Author Affiliations: Department of Biochemistry and Cell Biology
The Geisel School of Medicine at Dartmouth, Hanover, NH 03755
*Corresponding author
james.b.moseley@dartmouth.edu

Abstract: Control of cell size requires molecular size sensors that are coupled to the cell cycle. Rod-shaped fission yeast cells divide at a threshold size partly due to Cdr2 kinase, which forms nodes at the medial cell cortex where it inhibits the Cdk1-inhibitor Wee1. Pom1 kinase phosphorylates and inhibits Cdr2, and forms cortical concentration gradients from cell poles. Pom1 inhibits Cdr2 signaling to Wee1 specifically in small cells, but the time and place of their regulatory interactions were unclear. We show that Pom1 forms stable oligomeric clusters that dynamically sample the cell cortex. Binding frequency is patterned into a concentration gradient by the polarity landmarks Tea1 and Tea4. Pom1 clusters colocalize with Cdr2 nodes, forming a glucose-modulated inhibitory threshold against node activation. Our work reveals how Pom1-Cdr2-Wee1 operates in multiprotein clusters at the cortex to promote mitotic entry at a cell size that can be modified by nutrient availability.

Introduction:

Many cell types display a remarkable ability to maintain a constant size during rapid cycles of growth and division (Fantes and Nurse, 1977; Ginzberg et al., 2015; Jorgensen and Tyers, 2004; Lloyd, 2013). Such cell size control is a systems-level property that emerges from the integration of multiple size-dependent signal transduction pathways. Each signaling pathway is comprised of tunable biochemical parameters, including gene-expression and post-translational modifications such as protein phosphorylation (Alberghina et al., 2009). One major challenge in cell size research is to understand the biochemical mechanisms of signal transduction in each pathway, and what makes them size-dependent. These control systems can generate size homogeneity for a given cell type, but cell size is also an adaptable property. For example, nutritional cues and other environmental factors can alter cell size (Fantes and Nurse, 1977; Kelkar and Martin, 2015; Shiozaki, 2009; Yanagida Mitsuhiro et al., 2011). Thus, a second major challenge in cell size research is to understand how size-dependent signaling pathways respond to changes in cell metabolism and stress.

In eukaryotic cells, these signaling pathways lead to regulated activation of the conserved cyclin-dependent kinase Cdk1 (Harashima et al., 2013). Activated Cdk1 triggers mitotic entry and the cascade of events that lead to cell division (Gould and Nurse, 1989; Simanis and Nurse, 1986). The fission yeast *Schizosaccharomyces pombe* is an excellent model system to study size-dependent signaling pathways that regulate Cdk1. Genetic screens performed in past decades have identified many conserved factors that regulate Cdk1, but how these factors form size-dependent signaling pathways remains less clear. Fission yeast cells have a simple geometry that facilitates cell size studies. These cylindrical cells maintain a constant cell width, and grow by linear extension during interphase (Fantes and Nurse, 1977; Moreno et al., 1989). A network of cell polarity proteins positioned at cell tips restricts growth to these sites and maintains proper cell morphology (Chang and Martin, 2009). As a result, cell length doubles in one cell cycle, and many aspects of cell geometry scale with this increase in cell length (Gu and Oliferenko, 2019; Neumann and Nurse, 2007). Recent studies used cell shape mutants to show that fission yeast cells primarily measure surface area, not length or volume, for

cell size control (Facchetti et al., 2019; Pan et al., 2014). A critical next step is to understand how signaling pathways that regulate Cdk1 might operate at the cell surface in a size-dependent manner.

Cdk1 activity is established by the opposing activities of the inhibitory protein kinase Wee1, and the counteracting phosphatase Cdc25 (Gautier et al., 1991; Gould and Nurse, 1989; Kumagai and Dunphy, 1991; Russell and Nurse, 1986, 1987; Strausfeld et al., 1991). In fission yeast, mutations in Wee1, Cdc25, and their upstream regulators lead to changes in cell size. Separate mechanisms link cell size with regulation of Wee1 versus Cdc25. The cellular concentration of Cdc25 increases as cells grow during interphase (Keifenheim et al., 2017; Moreno et al., 1990). In contrast, the concentration of Wee1 remains constant during interphase, but it is progressively phosphorylated by the conserved inhibitory kinases Cdr1 and Cdr2 (Aligue et al., 1997; Breeding et al., 1998; Kanoh and Russell, 1998; Keifenheim et al., 2017; Lucena et al., 2017; Opalko and Moseley, 2017; Russell and Nurse, 1987; Wu and Russell, 1993; Young and Fantes, 1987). *cdr2* mutants fail to divide at a constant surface area, and instead divide according to cell volume or length (Facchetti et al., 2019). This change suggests that Cdr2-Cdr1-Wee1 signaling underlies the primary size-sensing pathway that measures cell surface area, while additional pathways related to volume and length are engaged in its absence. The localization of Cdr2, Cdr1, and Wee1 support this model **(Figure 1A)**: Cdr2 forms punctate oligomeric structures called nodes that stably bind to the medial cell cortex, and recruits Cdr1 to these sites (Akamatsu et al., 2014, 2017; Guzmán-Vendrell et al., 2015; Martin and Berthelot-Grosjean, 2009; Morrell et al., 2004; Moseley et al., 2009). Wee1 localizes primarily in the nucleus and spindle-pole body, where it encounters Cdk1 to prevent mitotic entry (Masuda et al., 2011; Moseley et al., 2009; Wu et al., 1996). In addition, Wee1 transiently visits cortical Cdr1/2 nodes in bursts that lead to inhibition of Wee1 kinase activity (Allard et al., 2018). The frequency and duration of these Wee1 bursts at Cdr1/2 nodes increase approximately twenty-fold as cells double in size (Allard et al., 2018), leading to size-dependent inhibition of Wee1 at the cell surface.

86 This size-dependent change in Wee1 bursting dynamics is encoded into the Cdr1-
87 Cdr2-Wee1 pathway at two proposed levels. First, increased Wee1 bursting depends
88 upon the doubling in number of Cdr1/2 nodes during one cell cycle, but this 2-fold increase
89 is smaller than the 20-fold increase in Wee1 bursting (Allard et al., 2018; Deng and
90 Moseley, 2013; Pan et al., 2014). Second, activation of Cdr2 increases as cells increase
91 in size (Deng et al., 2014). Cdr2 kinase activity is required for Wee1 localization to nodes,
92 and is controlled by the upstream kinase Pom1 (Allard et al., 2018; Moseley et al., 2009).
93 Pom1 directly phosphorylates and inhibits the activation of Cdr2 (Bhatia et al., 2014; Deng
94 et al., 2014; Kettenbach et al., 2015; Martin and Berthelot-Grosjean, 2009; Moseley et al.,
95 2009). Pom1 also phosphorylates a separate set of sites on Cdr2 to disrupt
96 oligomerization and membrane binding (Bhatia et al., 2014; Rincon et al., 2014). Pom1
97 regulation of Cdr2 increases the frequency and duration of Wee1 bursts at Cdr1/2 nodes,
98 but only in small cells (Allard et al., 2018). Consistent with this defect, *pom1*Δ cells divide
99 at a small size due to dysregulation of the Cdr2-Cdr1-Wee1 pathway (Bähler and Pringle,
100 1998; Bhatia et al., 2014; Martin and Berthelot-Grosjean, 2009; Moseley et al., 2009;
101 Wood and Nurse, 2013). Taken together, these results suggest a size-dependent
102 interaction between Pom1 and its substrate Cdr2. However, the location and timing of
103 Pom1 interactions with Cdr2 have remained poorly defined.
104
105 Pom1 localizes in a cortical spatial gradient that is enriched at cell tips, with a lower
106 concentration at the medial cell cortex, where its substrate Cdr2 forms nodes (Bähler and
107 Pringle, 1998; Bhatia et al., 2014; Martin and Berthelot-Grosjean, 2009; Moseley et al.,
108 2009; Pan et al., 2014). Thus, the majority of Pom1 and Cdr2 molecules in a cell are
109 spatially separated **(Figure 1A)**, raising the question of when and where they interact.
110 Several lines of evidence suggest that the spatial distributions of Pom1 and Cdr2 are
111 critical for the size-dependent signaling properties of this pathway, and suggest the lateral
112 cell cortex as the key interface. For example, ectopic targeting of Pom1 to the medial cell
113 cortex inhibits Cdr2 node formation and Cdr2-dependent cell size signaling (Martin and
114 Berthelot-Grosjean, 2009). Additionally, the Pom1 gradient is disrupted as part of a
115 cellular response to glucose deprivation, which leads to increased Pom1 concentration at
116 the lateral cortex where it delays mitotic entry (Kelkar and Martin, 2015). This result also

117 demonstrates that Pom1-Cdr2 signaling responds to environmental input to coordinate
118 cell size with nutrient availability. In this system, Pom1 functions analogously to an
119 intracellular morphogen, acting as a concentration-dependent and localization-controlled
120 inhibitor of Cdr2 nodes. However, levels of Pom1 at the medial cell cortex in wild-type
121 cells growing under steady state conditions are low, constant, and do not vary with cell
122 size (Bhatia et al., 2014; Pan et al., 2014). How Pom1 provides size-dependent input to
123 Cdr2 is unclear and requires analysis of their molecular dynamics at the lateral cell cortex.
124
125 Past studies have led to a model for Pom1 gradient formation driven by the binding
126 and diffusion of individual Pom1 molecules in the plasma membrane (Hachet et al., 2011;
127 Hersch et al., 2015; Saunders et al., 2012). Intriguingly, dynamic clusters of Pom1 have
128 also been observed and are proposed to form by unstable oligomerization of molecules
129 diffusing on the membrane (Hachet et al., 2011; Saunders et al., 2012). These clusters
130 are thought to form and decay rapidly, temporarily slowing Pom1 diffusion rates and
131 reducing noise in the gradient (Saunders et al., 2012). These clusters represent nano-
132 scale pockets of increased Pom1 concentration, but whether these clusters contribute to
133 regulation of Cdr2 nodes is unknown. Here, we combine biochemical and microscopy
134 approaches to show that the Pom1 gradient is comprised of these punctate clusters.
135 Pom1 clusters are stable oligomers that bind and release the membrane with minimal
136 lateral diffusion. These clusters bind more frequently at cell tips than at cell sides, resulting
137 in a concentration gradient. A portion of Pom1 clusters in the medial cell cortex colocalize
138 with Cdr2 nodes, and the ratio of Pom1 to Cdr2 at the medial cell cortex changes as a
139 function of cell size. When glucose is restricted, Pom1 clusters redistribute to the medial
140 cell cortex to prevent dramatic dysregulation of Wee1. Our work reveals that the Pom1-
141 Cdr2-Wee1 signaling pathway is organized as a series of cortical clusters. The relative
142 distribution of these clusters at the plasma membrane changes with cell size and glucose
143 availability, thus relaying cell surface area to the core cell cycle machinery in a nutrient-
144 controlled manner.
145
146

147 # Results:

148 **The Pom1 gradient is formed by transient cortical clusters**

149 We sought to examine the molecular dynamics of Pom1-Cdr2 signaling at the cell
150 cortex. As a starting point, we imaged Pom1 by TIRF microscopy, which selectively
151 excites fluorophores near the coverslip. Pom1 was tagged at the endogenous locus with
152 the bright and photostable fluorophore mNeonGreen (mNG). Surprisingly, along the
153 lateral cortex of interphase cells, Pom1-mNG was localized almost exclusively in discreet
154 clusters, with no apparent diffuse signal **(Figure 1B)**. In images from a single time-point,
155 Pom1 clusters formed a noisy concentration gradient **(Figure 1B,D)**. Time-averaging
156 produced a smoother gradient dotted by occasional clusters **(Figure 1B,D)**, similar to the
157 gradient observed by confocal microscopy **(Figure 1— figure supplement 1A,B)**. Pom1
158 clusters were highly dynamic **(Video 1)**. They appeared on the cell sides with a frequency
159 of ~2 $\mu m^{-2}s^{-1}$, and remained bound for less than 2 seconds on average **(Figure 1E,F)**.
160 During this brief cortical attachment, Pom1 clusters exhibited minimal diffusion which
161 lacked directionality, and instead appeared to diffuse randomly in submicron patches of
162 cortex **(Figure 1—figure supplement 2A,B,E)**. Mean squared displacement (MSD)
163 measurements were consistent with free diffusion of Pom1 clusters within submicron
164 corrals **(Figure 1—figure supplement 2A,B,C,D)** (Qian et al., 1991). The measured
165 diffusion coefficient ($D=0.134\pm0.017\mu m^2/s$) was slow for a membrane-associated protein
166 (Knight et al., 2010; Weiß et al., 2013), likely reflecting the large size and/or multiple
167 membrane contacts for oligomeric Pom1 clusters.

168

169 We next used "head-on" TIRF microscopy to image Pom1 at cell tips. Similar to
170 cell sides, Pom1-mNG localized at cell tips almost entirely in clusters **(Figure 1C)**. We
171 also used "head-on" confocal imaging to confirm that Pom1 localization in clusters at tips
172 was not an artifact of the TIRF approach **(Figure 1—figure supplement 1C)**; a
173 conclusion further supported by work using high resolution wide-field microscopy
174 (Dodgson et al., 2013). Compared to cell sides, Pom1 clusters appeared twice as
175 frequently at cell tips but with a similar cortical duration, again exhibiting minimal and non-
176 directional diffusion away from their binding site **(Figure 1E,F, Figure 1—figure**
177 **supplement 2E)**. Fluorescence intensity of individual clusters at cell tips and cell sides

178 were similar, although we detected a low number of brighter clusters at cell tips, likely
179 representing multiple diffraction-limited clusters **(Figure 1—figure supplement 1C,D,E)**.
180 From these data, we conclude that the Pom1 gradient is formed by patterning the
181 membrane binding frequency of cortical clusters along the long axis of the cell, rather
182 than by diffusion of Pom1 molecules from the cell tips to the cell side.
183
184 ***In vitro* analysis shows Pom1 exists in large, stable clusters**
185 Past work suggested that Pom1 structures assemble and disassemble at the
186 cortex through oligomerization of individual molecules diffusing in the plane of the
187 membrane (Saunders et al., 2012). However, our high-speed (20ms/frame) continuous
188 TIRF videos suggested that Pom1 clusters bind and release the cortex as a pre-formed
189 unit **(Figure 2—figure supplement 1A)**. Consistent with this possibility, in the rare cases
190 when we observed cell lysis events during TIRF imaging, Pom1 clusters remained intact
191 in extruded cytoplasm **(Figure 2A)**. This apparent stability while removed from the plasma
192 membrane led us to test the existence and properties of Pom1 clusters in detergent cell
193 extracts. Using TIRF microscopy, we observed clusters of Pom1-mNG in extracts made
194 from Pom1-mNG cells, but not from untagged wild-type cells **(Figure 2B)**. We next
195 examined the size of these Pom1 clusters by velocity sucrose gradient sedimentation. By
196 fractionating detergent cell extracts from *pom1-3xHA* cells, we found that most Pom1
197 exists in a large 60S complex, consistent with Pom1 clusters observed in cells. Fractions
198 6-8 containing this peak were dialyzed and centrifuged on a second sucrose gradient.
199 These pooled fractions again sedimented at 60S, indicating that they represent a stable
200 complex **(Figure 2C, Figure 2—figure supplement 2A,B,C)**.
201
202 Next, we tested the behavior of isolated Pom1 clusters on fluid artificial supported
203 lipid bilayers (SLBs) **(Figure 2D, Figure 2—figure supplement 1B)**. In this cell free-
204 system, Pom1-mNG clusters bound and released SLB lipids with strikingly similar
205 dynamics as in cells **(Figure 2E,F, Video 2)**. MSD measurements for Pom1 clusters on
206 SLBs revealed a diffusion coefficient similar to that measured in cells
207 (D_{cell}=0.134±0.017μm^2/s vs D_{SLB}= 0.168±0.018μm^2/s), but the relationship was linear over
208 the lifetime of most particles **(Figure 2—figure supplement 3A,B,C,D)**. These results

209 indicate that whereas membrane diffusion of Pom1 clusters in cells is confined within
210 microdomains, clusters can diffuse without confinement on synthetic bilayers. Dwell times
211 were increased for the kinase-dead mutant Pom1(K728R)-mNG, which was previously
212 shown to increase cortical Pom1 levels in cells **(Figure 2—figure supplement 1C).**
213 (Bähler and Pringle, 1998; Hachet et al., 2011). Pom1 clusters did not colocalize with
214 Cdr2 nodes in detergent extracts, suggesting they remain as separate structures **(Figure**
215 **2 – figure supplement 1D)**. Collectively, our TIRF microscopy and *in vitro* analysis of
216 Pom1 clusters support a model whereby the majority of cellular Pom1 protein is contained
217 within discreet, highly-stable oligomers that bind and release membranes with kinetics
218 dictated by their catalytic activity in a pattern that generates a concentration gradient.
219
220 Formation of clusters could represent an intrinsic property of Pom1 protein, or
221 alternatively might require additional cellular factors. To distinguish between these
222 possibilities, we expressed and purified GST-Pom1 from bacteria, and then performed
223 sucrose gradient centrifugation experiments. Recombinant GST-Pom1 sedimented in a
224 low molecular weight peak unlike Pom1 clusters from cells **(Figure 2G)**. Remarkably,
225 purified GST-Pom1 was assembled into a cluster-sized high molecular weight complex
226 by incubation with wild-type yeast detergent extract **(Figure 2G)**. Complex formation was
227 also induced by incubation of GST-Pom1 with *pom1*Δ cell extracts, meaning that
228 additional cellular factors drive this assembly process **(Figure 2G).** Once assembled,
229 Pom1 clusters are stable oligomeric complexes with intrinsic membrane-binding
230 properties that can be reconstituted *in vitro*. Additional cellular regulatory proteins are
231 likely to promote the binding of Pom1 clusters at cell tips, leading to the spatial gradient.
232
233 **Polarity landmarks pattern cortical dynamics of Pom1 clusters to shape the**
234 **gradient**
235 The key role of clusters in forming the Pom1 gradient led us to reexamine the role
236 of cell polarity landmark proteins Tea1 and Tea4. Both of these proteins localize at cell
237 tips and are required for proper Pom1 gradient formation (Hachet et al., 2011). However,
238 past studies have shown that Tea1 and Tea4 have distinct mechanistic roles: Tea4 is
239 required for localization of Pom1 to the cortex, whereas Tea1 is required for enrichment

240 of cortical Pom1 to the cell tip (Hachet et al., 2011). We first used sucrose gradient
241 centrifugation to test if either protein is required for assembly of Pom1 into stable
242 biochemical complexes. The sedimentation pattern of Pom1 clusters isolated from *tea1*Δ
243 and *tea4*Δ cells in velocity sucrose gradients is unchanged from wild-type cells,
244 suggesting that neither Tea1 nor Tea4 are required for assembly of Pom1 into stable
245 biochemical complexes **(Figure 3A)**. Rather, these regulators are likely to act
246 downstream of cluster assembly.
247
248 We next tested the localization and dynamics of Pom1-mNG in *tea1*Δ and *tea4*Δ
249 cells. We confirmed that Pom1 was absent from the cell cortex in confocal micrographs
250 of *tea4*Δ cells **(Figure 3—figure supplement 1A,** (Hachet et al., 2011)**)**. Surprisingly, we
251 did observe Pom1-mNG clusters throughout the cortex of *tea4*Δ cells by TIRF microscopy
252 **(Figure 3B)**. These binding events occurred with low frequency and short dwell times
253 **(Figure 3C,D, Figure 3—figure supplement 1B,C,D)**, which likely preclude their
254 detection by confocal microscopy. In contrast, confocal micrographs of Pom1-mNG in
255 *tea1*Δ cells confirmed even distribution around the entire cell cortex **(Figure 3—figure**
256 **supplement 1A,** (Hachet et al., 2011)**)**. In TIRF microscopy of *tea1*Δ cells, Pom1-mNG
257 clusters bound the cell cortex with the same frequency at cell sides and cell tips **(Figure**
258 **3B,C,D, Figure 3—figure supplement 1B,C,D)** resulting in enrichment of cortical Pom1
259 but not a gradient. Thus, Tea1 and Tea4 cooperate to promote localized membrane
260 binding but not assembly of Pom1 clusters. These spatial cues pattern the frequency and
261 binding duration of Pom1 cluster cortical interaction along the long axis of the cell to
262 generate a concentration gradient that emanates from cell tips.
263
264 **Pom1 clusters interact with Cdr2 nodes at the lateral cortex**
265 It has been unclear when and where Pom1 interacts with its inhibitory target Cdr2,
266 which localizes in cortical nodes positioned in the cell middle. Both Pom1 and Cdr2 are
267 enriched at the cortex, and their cytoplasmic concentrations do not change with cell size
268 **(Figure 4—figure supplement 1A,B,C,D,E)**. Furthermore, Cdr2 nodes and Pom1
269 clusters do not colocalize in cytoplasmic extracts, suggesting the cytoplasm is not the
270 location of their interaction **(Figure 2—figure supplement 1D)**. Since Pom1 clusters

271 appear to bind throughout the medial cell cortex, we used simultaneous two-color TIRF
272 microscopy to test colocalization of Pom1 clusters and Cdr2 nodes in this region of
273 overlap. We observed colocalization between Cdr2 nodes and some Pom1 clusters, as
274 well as Pom1 clusters that bound to the cortex without encountering a Cdr2 node **(Figure**
275 **4A)**. Thus, Pom1 clusters bind to the medial cortex in an apparently stochastic pattern
276 that can generate overlap with Cdr2 nodes. These patterns of colocalization were
277 apparent in both static images and time-lapse movies **(Figure 4A,B)**. Similar results were
278 obtained if different fluorophores were used to tag Pom1 and Cdr2, indicating that
279 colocalization is unlikely an artifact of the fluorescent tags **(Figure 4—figure supplement**
280 **2A,B)**. The frequency, dwell time, and displacement of Pom1 cortical clusters were
281 unaffected in *cdr2*Δ cells **(Figure 4—figure supplement 3A,B,C)**. These data suggest
282 that Pom1 interacts with its substrate Cdr2 when Pom1 clusters associate with Cdr2
283 nodes at the medial cell cortex.
284
285 Phosphorylation by Pom1 prevents activation of Cdr2 in small cells, thereby
286 contributing to cell size-dependent regulation of Wee1 and mitotic entry (Allard et al.,
287 2018). To place this genetic pathway in the cellular context of Pom1 clusters and Cdr2
288 nodes, we analyzed how these structures accumulate and colocalize as cells grow.
289 Intriguingly, the total number of both Cdr2 nodes and Pom1 clusters detected along entire
290 cell sides in TIRF images were equivalent for cells of a given size **(Figure 4C,D)**, and
291 both structures show a similar size-dependent doubling. We next restricted our analysis
292 to a 2μm x 2μm square ROI positioned at the cell middle, where Cdr2 nodes concentrate.
293 The local density of Cdr2 nodes in this region increased as a function of cell size,
294 consistent with past studies (Deng and Moseley, 2013; Pan et al., 2014). In contrast, the
295 density of Pom1 clusters in this region was largely independent of cell size **(Figure 4E)**.
296 In both TIRF and confocal images, the concentration of Pom1 protein and Pom1 clusters
297 decreased slightly as cells increase in size, but this trend was dwarfed by the cell size-
298 dependent increase in Cdr2 node density **(Figure 4E, Figure 4—figure supplement 3D)**.
299 Thus, as cells grow larger, the ratio of Pom1 to Cdr2 in the medial cell cortex changes to
300 favor Cdr2 because the densities of these two structures scale differently with cell size
301 **(Figure 4G)**.

302

303 We next tested how this density scaling affects colocalization of Pom1 clusters and
304 Cdr2 nodes as cells grow. Due to the increasing density of Cdr2 nodes, we observed an
305 increased number of colocalized Pom1 clusters and Cdr2 nodes at cell sides as cells
306 increase in size **(Figure 4F, Figure 4—figure supplement 3E)**. The increased
307 colocalization, combined with the constant density of Pom1 clusters, means that there
308 are less "free" Pom1 clusters as cells increase in size. Perhaps more importantly, the
309 number of "free" Cdr2 nodes increased as a function of cell size **(Figure 4—figure**
310 **supplement 3F)**. These free Cdr2 nodes are not occupied by an inhibitory Pom1 cluster,
311 and thus have increased potential to promote mitotic entry by inhibiting Wee1. In this
312 manner, Pom1 sets an inhibitory threshold that must be overcome by an increase in Cdr2
313 node density. The inhibitory threshold decreases slightly as cells grow, and functions
314 most effectively in small cells, where Pom1 was previously shown to inhibit downstream
315 signaling to Wee1 (Allard et al., 2018).
316

317 **Control of Pom1 cluster levels in the medial cell cortex**

318 Our results suggest that Pom1 sets an inhibitory threshold that opposes Cdr2
319 activation until cells reach an appropriate size for division. We hypothesized that the
320 strength of the Pom1 inhibitory threshold could be tuned by altering the concentration of
321 Pom1 cortical clusters in the cell middle. To increase the abundance of Pom1 clusters in
322 the cell middle, we grew Pom1-mNG cells in low glucose media. In low glucose
323 conditions, the fission yeast microtubule cytoskeleton depolymerizes, which leads to
324 Pom1 redistribution to the lateral cell cortex where it delays mitotic entry (Kelkar and
325 Martin, 2015). In time-lapse TIRF microscopy experiments, we observed increased
326 numbers of discreet Pom1 clusters at the lateral cell cortex under low glucose conditions
327 **(Figure 5A)**. These clusters bound to the lateral cortex more frequently than under normal
328 glucose conditions, but the average dwell time was unaffected **(Figure 5B,C)**. This
329 increased on-rate leads to accumulation of Pom1 clusters at the medial cell cortex.
330

331 We tested how increased numbers of Pom1 clusters at the lateral cell cortex affect
332 Cdr2 nodes using TIRF microscopy. In low glucose conditions, the number of Cdr2 nodes

333 measured per cell was largely unchanged. However, we observed a significant reduction
334 in the number of Cdr2 molecules per node, and in the overall concentration of Cdr2 at the
335 medial cortex **(Figure 5D,E,F, Figure 5—figure supplement 1A,B,C)**. Low glucose did
336 not affect Cdr2 nodes in *pom1*Δ cells, so these effects are Pom1-dependent **(Figure**
337 **5D,E,F)**. Thus, Pom1 redistribution to the lateral cortex under low glucose is required to
338 induce partial disassembly of each Cdr2 node. We quantified how this redistribution effect
339 scales with glucose levels. As glucose was reduced, Pom1 concentration decreased at
340 cell tips and increased at cell sides **(Figure 6A,C,D)**. Pom1 concentration at the lateral
341 cortex therefore serves as a cellular indicator of glucose availability. In contrast, Cdr2
342 concentration increased at cell tips and decreased at cell sides **(Figure 6B,C,D)**. The
343 concentrations of Pom1 and Cdr2 at cell sides were nearly perfectly anti-correlated
344 (Pearson's r=-0.9352, *p*=0.0006) **(Figure 6E,F)**. We conclude that the increasing
345 frequency of Pom1 cluster binding at the lateral cell cortex leads to a reduced number of
346 Cdr2 molecules per node.
347
348 **Pom1 disrupts Wee1 bursting under glucose deprivation**
349 We next examined the downstream effects of altered Pom1-Cdr2 signaling in low
350 glucose by using TIRF microscopy to monitor the previously described bursts of Wee1-
351 mNG localization at Cdr2 nodes (Allard et al., 2018). In wild-type cells, both the frequency
352 and duration of Wee1 bursts increased linearly with cell size, consistent with increased
353 inhibition of Wee1 as cells grow **(Figure 7A,B, Supplemental Table 1, Supplemental**
354 **Table 2)**. In low glucose, the frequency of Wee1-mNG bursts still scaled with cell size as
355 in normal glucose. However, the duration of each burst was uniformly short and
356 independent of cell size **(Figure 7A,B, Supplemental Table 1, Supplemental Table 2)**.
357 Therefore, glucose modulates how long Wee1 molecules stay at inhibitory Cdr2 nodes.
358 These same properties were seen for Wee1-mNG bursts in kinase-dead *cdr2(E177A)*
359 mutant cells grown in normal glucose **(Figure 7—figure supplement 1A,B,**
360 **Supplemental Table 1, Supplemental Table 2)**. These results indicate that Cdr2 kinase
361 activity is required to retain Wee1 at nodes, but not for the initial binding event. Further,
362 they demonstrate that low glucose phenocopies the kinase-dead *cdr2(E177A)* mutant,
363 consistent with Pom1-dependent inhibition of Cdr2 kinase activity.

These results suggested that reduced Wee1 bursting in low glucose might require Pom1 redistribution. We tested this idea by examining the glucose dependency of Wee1 localization to nodes in *pom1*Δ cells. In *pom1*Δ cells growing under high glucose, the Wee1 burst frequency scales with cell size but Wee1 burst duration is uniformly high and independent of cell size **(Figure 7A,C, Supplemental Table 1, Supplemental Table 2)**. Unlike wild type cells, which suppress Wee1 bursts in low glucose, *pom1*Δ cells show a striking increase in Wee1 bursts under low glucose. This increase is not caused by burst duration, which was independent of both cell size and glucose concentration in *pom1*Δ cells **(Figure 7C, Supplemental Table 1, Supplemental Table 2)**. Rather, we measured increased Wee1-mNG burst frequency in low glucose *pom1*Δ cells **(Figure 7A,C, Supplemental Table 1, Supplemental Table 2)**. The reason for this increase is unknown, and suggests the existence of additional glucose-regulated pathways that operate on Cdr2-Wee1 signaling.

Wee1 localization at Cdr2 nodes leads to its inhibitory phosphorylation by Cdr2 and the related kinase Cdr1. To test how our microscopy results connect with Wee1 phosphorylation status, we analyzed phosphorylation-dependent shifts of Wee1 migration using western blots **(Figure 7D)**. In high glucose, Wee1 migrates as a smear of phosphorylated isoforms (Allard et al., 2018; Lucena et al., 2017). The upper, hyperphosphorylated forms are increased in *pom1*Δ cells but absent in *cdr2*Δ cells. This hyperphosphorylated Wee1 is lost in wild-type cells grown in low glucose, consistent with reduced bursts of Wee1 localization to nodes. In contrast, Wee1 appears even more hyperphosphorylated in *pom1*Δ cells grown under low glucose. This result suggests that Pom1 prevents phospho-inactivation of Wee1 in response to low glucose. These combined experiments support a model where Pom1 redistribution to the lateral cell cortex inactivates Cdr2 nodes to relieve inhibition of Wee1 under low glucose conditions.

Discussion:

In this study, we have shown that the Pom1 concentration gradient is generated by oligomeric Pom1 clusters that rapidly bind and release from the plasma membrane.

395 These clusters bind more frequently at cell tips versus cell sides in high glucose media,
396 while their binding rate is increased at cell sides in low glucose media. At the medial cell
397 cortex, these clusters overlap with their inhibitory target Cdr2, which localizes in static
398 oligomeric nodes. More Cdr2 nodes are free from Pom1 inhibition as cells grow larger
399 due to different density scaling of these two structures at the medial cell cortex. Our TIRF-
400 based colocalization experiments on these structures were limited to short periods of time
401 to avoid photobleaching, partly caused by the imaging conditions needed to observe
402 these highly dynamic Pom1 clusters. Nevertheless, Pom1 clusters colocalized with Cdr2
403 nodes even over these short timescales. Given the high frequency of Pom1 cluster
404 binding, we expect that many more colocalization events occur between Cdr2 nodes and
405 Pom1 clusters during the course of a full cell cycle, with the potential for Pom1 clusters
406 to visit each Cdr2 node multiple times. Thus, these rapid dynamics of Pom1 clusters
407 interacting with Cdr2 nodes may be integrated in time throughout the cell cycle. It appears
408 likely that the most critical temporal window for Pom1-Cdr2 interactions occurs during
409 early G2, as *pom1*Δ show defects in Cdr2-Wee1 signaling specifically in small cells (Allard
410 et al., 2018). It will be interesting to determine how these rapid interactions in small cells
411 are integrated into the mitotic entry decision, which occurs later in the cell cycle when
412 cells are longer.
413
414 **Molecular clusters are widespread in signal transduction**
415 The Pom1-Cdr2-Wee1 signaling pathway appears to function entirely within the
416 confines of oligomeric protein clusters at the plasma membrane. The development of
417 imaging technologies with increased signal-to-noise and spatial and temporal resolution
418 has enabled the discovery of protein clustering as a paradigm in signaling. As a result, a
419 growing number of signaling events and proteins have been found in similar clustered
420 structures that are referred to as nanodomains, clusters, nanoclusters, and nodes, among
421 other names. Such structures have been shown to operate in polarization of the *C.*
422 *elegans* zygote, signal transduction nanodomains at the plant plasma membrane, Ras
423 isoform-specific signaling, bacterial chemotactic receptors, and both B-cell and T-cell
424 receptors (Bray et al., 1998; Dickinson et al., 2017; Douglass and Vale, 2005; Duke and
425 Bray, 1999; Falke, 2002; Gronnier et al., 2017; Liu et al., 2016; Maity et al., 2015; Munro,

426 2017; Rodriguez et al., 2017; Wang et al., 2017; Zhou and Hancock, 2015). These T cell
427 receptor clusters enrich downstream kinases while excluding phosphatases (Su et al.,
428 2016), a mechanism that could relate to concentrated clusters of the kinases Pom1 and
429 Cdr2. In addition, theoretical work has suggested that clustering can reduce noise by
430 generating reaction bursts (Kalay et al., 2012), which have the capacity to overcome
431 inhibitory thresholds, such as those imparted by phosphatases, more effectively than a
432 system driven by gradual accumulation of signal. Insight into the functional role of
433 clustering for Pom1-Cdr2-Wee1 will require additional *in vivo* analysis combined with *in*
434 *vitro* reconstitution. We have shown that Pom1 clusters remain stable through
435 biochemical enrichment, and isolated clusters exhibit the same membrane-binding
436 properties *in vitro* as in cells. Past work has demonstrated Cdr2 nodes also remain stable
437 through biochemical fractionation (Allard et al., 2018), providing the necessary tools for
438 future dissection of the pathway in a reconstituted system.
439
440 **A new model for cortical gradient formation**
441 Our work has shown that Pom1 clusters bind to the cell cortex with different
442 frequencies along the long axis of the cell, resulting in a concentration gradient. Past work
443 suggested single Pom1 molecules (or small oligomers) bind to the membrane at tips, and
444 then diffuse away from the tip before dissociating (Hachet et al., 2011; Saunders et al.,
445 2012). Clusters were proposed to dynamically assemble and disassemble at the cortex
446 from this diffusing population (Saunders et al., 2012). Our findings suggest a new model
447 for gradient formation, which is distinct from this previous model in four ways. First, we
448 found that clusters themselves form a concentration gradient that emanates from the cell
449 tips. Second, our combined imaging and biochemical approaches demonstrated that
450 clusters are stable complexes that bind and rapidly release from the membrane. Third,
451 we did not observe extensive diffusion by complexes bound to the membrane. It remains
452 possible that smaller, diffusing Pom1 complexes or single molecules were not detected
453 by our imaging approach, but we favor a model where diffusion is limited to short, non-
454 directional movements that do not contribute to gradient formation. Fourth, the key step
455 in gradient formation is a positional system that increases the on-rate for Pom1 clusters
456 at cell tips versus the cell middle. Concentration gradients are found across vast size

457 scales in biology, so the mechanism of gradient formation by Pom1 clusters may have
458 broad implications. It is also important to note that the spatial gradient of on-rates for
459 Pom1 clusters binding to the cortex may depend on a concentration gradient of specific
460 lipids in the plasma membrane. In support of this hypothesis, Pom1 binds to
461 phosphatidylserine *in vitro* (Hachet et al., 2011), and this lipid is enriched at the tips of
462 growing fission yeast cells (Haupt and Minc, 2017). Thus, further investigation of these
463 lipids and their localization dynamics could reveal additional layers of this morphogen-like
464 gradient.
465
466 We found that the polarity landmarks Tea1 and Tea4 provide the positional
467 information for Pom1 clusters to form a concentration gradient. Past work has shown that
468 Pom1 localizes homogenously throughout the cortex in *tea1*Δ cells, and does not localize
469 to the cortex in *tea4*Δ cells (Bähler and Pringle, 1998; Hachet et al., 2011). Based on
470 these and other results, Tea1 was proposed to recruit Tea4 to cell tips, where it promotes
471 cortical loading of Pom1 molecules. Several results suggest that additional mechanisms
472 may contribute to gradient formation. For example, we found that Pom1 clusters still bind
473 to the cortex in *tea4*Δ cells but for very short durations. Past work has also shown that
474 Tea1 and Tea4 form cortical clusters that co-localize at cell tips, but these Tea1-Tea4
475 clusters do not co-localize with Pom1 clusters (Dodgson et al., 2013). Thus, Tea1-Tea4
476 may pattern binding of Pom1 clusters to the cortex through an additional mechanism. For
477 example, Tea1 and Tea4 have been shown to assemble sterol-enriched lipid domains at
478 cell tips when cells initiate polarization following exit from starvation (Makushok et al.,
479 2016). Sterols and phosphatidylserine are thought to form a common membrane domain
480 in fission yeast, suggesting that these proteins could act through the recruitment and
481 organization of lipids to generate cortical domains permissive for Pom1 cluster binding
482 (Haupt and Minc, 2017; Makushok et al., 2016).
483
484 **Adjustable Pom1 gradients regulate mitotic entry**
485 We propose an integrated mechanism for fission yeast cell size sensing in which
486 Cdr2 acts as an important sensor of cell size that is dynamically antagonized by cortical
487 Pom1 **(Figure 8)**. Pom1 clusters bind to the medial cell cortex in a manner that can

488 overlap with Cdr2 nodes. These dynamic Pom1 clusters and static Cdr2 cortical nodes
489 suggest a system that monitors surface expansion, consistent with the notion that fission
490 yeast cells monitor surface area as the primary determinant of size at division (Facchetti
491 et al., 2019; Pan et al., 2014). As cells grow, the density of Pom1 clusters in the cell
492 middle decreases slightly due to their binding preference at cell tips. In contrast, the
493 density of Cdr2 nodes doubles to overcome this inhibitory Pom1 threshold. The density
494 of Pom1 clusters and the resulting inhibitory threshold can be modulated by glucose
495 availability, consistent with past work (Kelkar and Martin, 2015). As fission yeast cells
496 begin to starve due to depletion of nutrients such as glucose, their length at division
497 progressively decreases and the length of the cell cycle increases (Pluskal et al., 2011;
498 Yanagida Mitsuhiro et al., 2011). The Pom-Cdr2 network has a prominent role in this
499 nutrient modulation, suggesting that it may represent a key physiological role for the
500 pathway (Kelkar and Martin, 2015). We found that the size dependence of Wee1
501 localization bursts to Cdr2 nodes, which facilitate Wee1 inhibition, was dampened in low
502 glucose conditions. Re-localization of Pom1 clusters to the medial cortex mediates this
503 response. However, for *pom1*Δ mutants in low glucose, Wee1 localization to nodes
504 exceeds even wild type cells in high glucose. This result indicates that additional
505 mechanisms contribute to Wee1 regulation in low glucose, for example Wee1 nuclear
506 transport could be altered under these conditions. Thus, Pom1-Cdr2 signal transduction
507 serves two functions: (1) Under steady-state growth conditions, Pom1 and Cdr2
508 cooperate to measure cell size and ensure that cells divide only when they have grown
509 large enough. In this context, the Pom1 threshold is only strong enough to inhibit Cdr2
510 signaling in small cells, where node density is low. In this manner, Pom1 prevents
511 precocious entry into mitosis. (2) Under glucose restriction, Pom1 and Cdr2 cooperate
512 to integrate information about both cell size and glucose availability, and signal that
513 information to the core cell cycle machinery.
514
515 **The Pom1 gradient as a read-out for cell polarity**
516 More broadly, our study reveals the adjustable nature of the concentration gradient
517 formed by Pom1 clusters. Concentration of Pom1 clusters at cell tips reads out the polarity
518 state of the cell for downstream signaling by Cdr2 and Wee1. Conditions that alter the

519 polarized growth state of the cell would lead to changes in the gradient of Pom1 clusters,
520 resulting in altered cell size at division. This dynamic system appears to operate in a
521 manner that depends on both cell size and nutrient availability. Identification of additional
522 growth and environmental conditions that alter the relative distributions of Pom1 clusters
523 and Cdr2 nodes, and determination of how they connect with other cell cycle signaling
524 pathways, may reveal new mechanisms for nutrient modulation of cell size control.
525

526 **Integration of the Pom1-Cdr2-Wee1 pathway with other sizing mechanisms**

527 Pom1-Cdr2-Wee1 signaling is cell size dependent but is not the only pathway that
528 contributes to the overall cell size control network. Intriguingly, a recent study reported
529 that *cdr2*Δ cells no longer divide based on accumulation of a threshold surface area and
530 instead revert to a secondary mechanism of cell size control based on volume sensing
531 (Facchetti et al., 2019). These results demonstrate that cells use different signal
532 transduction networks to measure different aspects of their size. Whereas the Pom1-Cdr2
533 network is well suited to measure cortical surface area, size-control systems that measure
534 other aspects of size would require different signaling logic. Theoretically, mechanisms
535 for cell volume sensing could depend on proteins whose concentrations do not scale
536 linearly with cell size. Such mechanisms are thought to underlie cell size control in other
537 organisms, such as the budding yeast, where growth-dependent dilution of the
538 transcriptional repressor Whi5 is thought to underlie G_1/S size control (Schmoller et al.,
539 2015). One possible candidate for cellular volume sensing in fission yeast is Cdc25, which
540 increases in concentration with cell size (Keifenheim et al., 2017; Moreno et al., 1990).
541 These mechanisms are attractive candidates for volume sensors because cytoplasmic
542 concentration is independent of cell geometry. The existence of sizing mechanisms that
543 measure other aspects of cell size, and function independently of the Pom1-Cdr2 surface
544 area sensing network, underscores that cell size is a systems level property controlled by
545 multiple signaling pathways. Thus, it remains important to discover size-dependent
546 signaling mechanisms within each individual pathway, as a step towards understanding
547 the integration of multiple pathways into a larger size control system.
548

549

550 # Materials and Methods:

551 **Key Resources Table**

Reagent type (species) or resource	Designation	Source or reference	Identifiers	Additional information
strain, strain background ()	*pom1-yomNeonGreen::hphR*	This Paper	JM4496	
strain, strain background ()	*pom1-3HA::hphR ura4-D18 leu1-32 h+*	PN948	JM797	Paul Nurse Lab
strain, strain background ()	*pom1Δ::natR h-*	Lab Stock	JM966	
strain, strain background ()	*pom1-m2-yomNeonGreen::hphR ura4-D18 leu1-32 h-*	This Paper	JM5412	
strain, strain background ()	*pom1-3HA::hphR tea1Δ::ura4+ ura4-D18*	This Paper	JM5414	
strain, strain background ()	*pom1-3HA::hphR tea4Δ::kanMX6*	This Paper	JM5415	
strain, strain background ()	*pom1-yomNeonGreen::hphR tea1Δ::kanMX6*	This Paper	JM4792	
strain, strain background ()	*pom1-yomNeonGreen::hphR tea4Δ::kanMX6*	This Paper	JM4791	
strain, strain background ()	*pom1-yomNeonGreen::hphR cdr2-tagRFP-t::hphR*	This Paper	JM5373	
strain, strain background ()	*cdr2-yomNeonGreen::hphR h-*	Lab Stock	JM4493	

strain, strain background ()	*wee1-yomNeonGreen::hphR cdr2Δ::natR*	Lab Stock	JM4525	
strain, strain background ()	*cdr2-yomNeonGreen::hphR pom1-tdTomato::natR*	This Study	JM5135	
strain, strain background ()	*cdr2-mEGFP::kanMX6 ura4-D18 leu1-32 ade6-m210 h+*	Lab Stock	JM346	
strain, strain background ()	*cdr2-yomNeonGreen::hphR pom1Δ::natR*	This Paper	JM5359	
strain, strain background ()	*wee1-yomNeonGreen::hphR h-*	Lab Stock	JM4495	
strain, strain background ()	*wee1-yomNeonGreen::hphR pom1Δ::kanMX6*	Lab Stock	JM4527	
strain, strain background ()	*972 h-*	PN1	JM366	Paul Nurse lab
strain, strain background ()	*cdr2Δ::natR ura4-D18 leu1-32 h+*	Lab Stock	JM600	
strain, strain background ()	*wee1-yomNeonGreen::hphR cdr2(E177A)*	Lab Stock	JM4578	
recombinant DNA reagent	pFA6a-yomNeonGreen::hphR	Lab Stock	pJM1344	
recombinant DNA reagent	pFA6a-tdTomato::natR	Lab Stock	pJM248	
recombinant DNA reagent	pFA6a-yomTagRFP-T::hphR	Lab Stock	pJM1221	Derived from Addgene Plasmid 44842

recombinant DNA reagent	pFA6a-mEGFP::kanMX6	Lab Stock	pJM228	
recombinant DNA reagent	pFA6a-3HA::hphR	Lab Stock	pJM216	
antibody	anti-HA (mouse monoclonal)	Covance	MMS-101R	WB (1:3000)
antibody	anti-GST (rabbit polycolonal)	This Paper		WB (1:3000)
chemical compound, drug	1,2-dioleoyl-sn-glycero-3-phospho-L-serine (sodium salt)	Avanti Polar Lipids	840035C	18:1 DOPS or "PS"
chemical compound, drug	1,2-dioleoyl-sn-glycero-3-phosphoethanolamine-N-(lissamine rhodamine B sulfonyl) (ammonium salt)	Avanti Polar Lipids	810150C	18:1 Liss Rhod PE
chemical compound, drug	1,2-dioleoyl-sn-glycero-3-phosphocholine	Avanti Polar Lipids	850375C	18:1 (Δ9-Cis) PC (DOPC) or "PC"

552

553 **Strain Construction and Media**

554 Standard *S. pombe* media and methods were used (Moreno et al., 1991). Strains
555 used in this study are listed in the Key Resources Table. Gene tagging and deletion were
556 performed using PCR and homologous recombination (Bähler et al., 1998). The
557 mNeonGreen (mNG) sequence was used under license from Allele Biotechnology.
558 Addgene Plasmid 44842 (pFA6a-link-yoTagRFP-T-SpHis5) was a gift from Wendell Lim
559 & Kurt Thorn (Addgene plasmid # 44842; http://n2t.net/addgene:44842 ;
560 RRID:Addgene_44842).

561

562 **TIRF Microscopy and Analysis**

563 Pom1 clusters and node components were imaged using simultaneous dual-color
564 total internal reflection fluorescence (TIRF) microscopy to limit excitation of fluorophores

565 to those nearest to coverslip. Imaging was performed on a commercially available TIRF
566 microscope (Micro Video Instruments) composed of a Nikon Eclipse Ti microscope base
567 equipped with a 100x Nikon Apo TIRF NA 1.49 objective and a two-camera imaging
568 adaptor (Tu-CAM, Andor Technlogy) containing a dichroic and polarization filters
569 (Semrock FF580-FDi01-25x36, FF02-525/40-25, FF01-640/40-25) to split red and green
570 signal between two aligned Andor iXon electron-multiplied CCD cameras (Andor
571 Technology). Red/green beam alignment was performed prior to imaging using a
572 TetraSpeck Fluorescent Microsphere size kit (Thermofisher).
573
574 Standard #1.5 glass coverslips were RCA cleaned before use to remove
575 fluorescent debris. Cells were grown in EMM4S, and washed into fresh EMM4S
576 immediately before imaging to remove auto-fluorescent debris resulting from overnight
577 culture. Cells were imaged in EMM4S media on glass slides at ambient temperature.
578 Individual slides were used for no more than five minutes to prevent cells from exhausting
579 nutrients or oxygen. Agar pads were not used due to increased background fluorescence.
580 Image analysis and processing was performed using ImageJ2 (NIH).
581
582 **"Head-On" Tip Imaging**
583 "Head-On" or "Tip" imaging was performed using a protocol modified from
584 (Dodgson et al., 2013). Custom micro-well coverslips or Ibidi Sticky-Slide VI channels
585 (Ibidi, Martinsried, Germany) were coated with BS-I lectin (1mg/mL in water) by incubation
586 for 30 minutes and washed 3X with water to remove non-adherent lectin. Cells were then
587 added to the imaging chambers and allowed to settle to the cover-slip bottom where they
588 adhere to the lectin. Cells oriented with the long axis perpendicular to the coverslip were
589 identified using brightfield prior to fluorescence imaging.
590
591 **Spinning Disc Microscopy and Analysis**
592 Spinning-disc confocal imaging was performed using a commercially available
593 system (Micro Video Instruments, Avon, MA) featuring a Nikon Eclipse Ti base equipped
594 with an Andor CSU-W1 two-camera spinning disc module, dual Zyla sCMOS cameras
595 (Andor, South Windsor, CT) an Andor ILE laser module, and a Nikon 100X Plan Apo λ

596 1.45 oil immersion objective. Cells were imaged in EMM4S media on glass slides at
597 ambient temperature unless otherwise noted.
598
599 **Airyscan Super-Resolution Microscopy and Analysis**
600 To achieve maximum resolution and sensitivity, fluorescence intensity of Pom1
601 clusters on both cell sides and cell tips was measured using a Zeiss Airyscan microscope
602 **(Figure 1—figure supplement 1C,D,E)**, composed of a Zeiss LSM-880 laser scanning
603 confocal microscope (Zeiss, Oberkochen, Germany) equipped with 100X alpha Plan-
604 Apochromat/NA 1.46 Oil DIC M27 Elyra objective, Airyscan super-resolution module and
605 GaAsP Detectors, and Zen Blue acquisition software using the Super-resolution mode
606 with pin-hole size of 1.2 airy-units to prioritize resolution. Z-volumes of 16 slices with
607 0.19μm spacing for high spatial resolution in all dimensions were centered on the cell
608 cortex closest to the coverslip. Airyscan images were processed in Zeiss Zen Blue
609 software, and quantification was performed on sum projections of Airyscan reconstructed
610 stacks.
611
612 **Single Particle Tracking**
613 Image analysis and processing was performed using ImageJ2 (NIH). Cdr2 node
614 numbers and Pom1/Wee1 clusters number, frequency and binding duration were
615 quantified using the Trackmate plugin (Tinevez et al., 2017) to analyze TIRF microscopy
616 movies. Due to variable fluorescence intensity in different TIRF fields and images,
617 thresholding parameters were determined separately for each image, and accuracy was
618 confirmed by visual inspection to ensure that only nodes/clusters were counted and that
619 no nodes/clusters were omitted. For Wee1 burst and Pom1 cluster tracking, Particle
620 Diameter was set to 0.3 microns (approximate XY resolution), with Maximum Gap Linking
621 set to 2 frames, and Linking Range for particle tracking was set to 0.15 microns. Lookup
622 table was adjusted to fire for some images to emphasize signal intensities. For Pom1
623 cluster tracking, analysis was restricted to 2μm x 2μm square ROIs positioned at the cell
624 middle or tip.
625
626 **Colocalization Analysis**

627 Colocalization analysis of Cdr2 nodes and Pom1 clusters as in **Figure 4F,G** and
628 **Figure 4—figure supplement 2E,F** was performed using two-color simultaneous TIRF
629 microscopy images as in **Figure 4A**. Analysis was restricted to 2μm^2 square ROIs
630 positioned at the cell middle. The spot detection algorithm in the Trackmate plugin
631 (Tinevez et al., 2017) for ImageJ2 was used to assign 0.3 μm diameter circular ROIs to
632 Cdr2 nodes (cyan) and Pom1 clusters (magenta) in images as in **Figure 4F**. Pom1 and
633 Cdr2 structures were counted as colocalized if the centroids of their respective ROIs were
634 spaced <150nm apart (yellow ROI pairs in **Figure 4F**.
635
636 **Mean Squared Displacement**
637 Mean Squared Displacement analysis and calculation of diffusion coefficients were
638 performed using the MATLAB (MathWorks, Natick, MA) class @msdanalyzer developed
639 in (Tarantino et al., 2014). Briefly, single-particle traces of high-speed (100ms acquisition)
640 TIRFM videos were generated using the Trackmate plugin for ImageJ2 as described
641 above and were then exported to MATLAB for further analysis. @msdanalyzer was then
642 used to plot and calculate MSD for each particle trace, plot the MSD curves, compute and
643 fit the mean MSD curve, and compute the diffusion coefficient.
644
645 **Pom1 Purification**
646 The full length Pom1 sequence was purified as follows: Pom1 sequence was
647 subcloned into pGEX6P1 vector using the Xho1 restriction site and expressed as a GST-
648 fusion protein in *Escherichia coli* strain BL21(DE3). Transformants were cultured to log-
649 phase at 37˚C, followed by a shift to 25˚C for 30 minutes. Expression was then induced
650 by addition of 1-thio-β-D-galactopyranoside to 200μM, followed by growth for an
651 additional 3 hours at 25˚C. Cells were harvested by centrifugation and lysed by passing
652 them twice through a French press in lysis buffer (1xPBS, 100mM NaCl, 1mM DTT, and
653 complete EDTA-free protease inhibitor tablets (1 tablet/50mL Buffer) (Roche, Basel,
654 Switzerland)). Following lysis, Triton-X 100 was added to 1% V/V. Lysates were then
655 cleared by centrifugation for 10 minutes at 12,000 x g at 4˚C in a Sorval SS-34 fixed-angle
656 rotor (Thermo Scientific, Waltham, MA). The supernatant was then incubated with
657 glutathione-agarose (Sigma Aldrich, St. Louis, MO) for 2h at 4˚C. 20 mM glutathione (pH

658 8.0) was used to elute purified protein, and the eluate was dialyzed overnight at 4˚C into
659 10mM Tris-HCl, pH8 + 5% V/V glycerol.
660
661 **Preparation of Yeast Extracts**
662 Fission yeast detergent extracts were prepared by growing 1.5L cells to mid-log
663 phase (OD ~0.3), and then washed twice with 50mL Node Isolation Buffer (NIB – 50mM
664 HEPES, 100mM KCl, 1mM $MgCl_2$, 1mM EDTA, pH 7.5) (Allard et al., 2018). Next, we
665 resuspended the pellet in an equal volume of 2X NIB (W/V) containing a
666 protease/phosphatase inhibitor cocktail (10µL/mL 200x PI, 50µL/mL 1M β-glycerol
667 phosphate, 50µL/mL 1M NaF, 2.5 µL/mL 200mM PMSF, 1mM DTT), and snap froze the
668 resuspension as pellets by pipetting drop-wise into a liquid nitrogen bath. Then, yeast
669 pellets were ground using liquid-nitrogen chilled coffee-grinders for 2 min, and collected
670 into chilled falcon tubes and stored at -80˚C. 1.5g of frozen yeast powder was then thawed
671 on ice, and Triton X-100 was added to a final concentration of 1%, and the extracts were
672 mixed by gentle pipetting. Extracts were then centrifuged at 4˚C for 10min at 20,000 x g
673 to yield a low speed supernatant, which were then used for subsequent experiments.
674
675 **Sucrose Gradient Ultracentrifugation**
676 Discontinuous sucrose gradients were prepared in 14 x 89mm Ultra Clear
677 Ultracentrifuge tubes (Beckman Coulter, Brea, CA) by layering 5 – 23% (top to bottom)
678 sucrose in NIB + 1% Triton X-100 in 0.37mL steps of 2% sucrose increments. 700µL of
679 yeast extract or recombinant protein diluted in NIB Buffer was then added to the top of
680 the gradient. Sucrose gradients were centrifuged at 100k x g (50kRPM) in a Beckman L8-
681 M ultracentrifuge for 2hr at 4˚C in a chilled SW60ti swinging bucket rotor. 0.5mL gradient
682 fractions were collected from the top by hand, vortexed, and 100µL of each fraction was
683 mixed 2:1 in 3X SDS-PAGE sample buffer (65 mM Tris pH 6.8, 3% SDS, 10% glycerol,
684 10% 2-mercaptoethanol, 50 mM NaF, 50 mM β-glycerophosphate, 1 mM sodium
685 orthovanadate) and boiled for 5 min. Samples were then subjected to SDS-PAGE and
686 western blotting or Coomassie staining. To calculate S-values of sedimentation peaks
687 from western blot signal intensities, mean band intensities were measured using Image
688 Studio Lite (LICOR, Lincoln, NE), and Gaussian Curves were fit to these values. The peak

689 of the Gaussian for each sedimentation peak of each protein was used to assign the
690 known or interpolated S-value.
691
692 **Western Blotting**
693 For western blots, cells were lysed in 150 µl of 3X SDS-PAGE sample buffer with
694 glass beads in a Mini-beadbeater-16 (Biospec, Bartlesville, OK) for 2 minutes. Gels were
695 run at a constant 20 mAmps until 75kDa marker was at the bottom of the gel. Blots were
696 probed with anti-HA (Covance, Princeton, NJ) or homemade anti-GST. For monitoring
697 Wee1 phosphorylation, samples were run on an SDS-PAGE gel containing 6%
698 acrylamide and 0.02% bisacrylamide, and then probed with a homemade anti-Wee1
699 antibody (Allard et al., 2018).
700
701 **Supported Lipid Bilayers**
702 To prepare supported lipid bilayers, we first prepared small unilamellar vesicles
703 (SUVs) composed of three lipids: (1) DOPC (18:1 (Delta9) Cis PC - 1,2 Dioleoyl-sn-
704 glycero-3-phosphocholine), (2) DOPS (18:1 PS - 1,2-Dioleoyl-sn-Glycero-3-[Phospho-L-
705 Serine]), and (3) fluorescent 18:1 Liss Rhod PE (1,2-dioleoyl-sn-glycero-3-
706 phosphoethanolamine-N-(lissamine rhodamine B sulfonyl). All lipids were dissolved in
707 chloroform (Avanti, Alabaster, AL). 2µmol total lipid with the desired molar ratios were
708 mixed in glass vials with PTFE coated caps, which had been RCA cleaned and rinsed
709 three times with chloroform before use. Excess chloroform was evaporated in a vacuum
710 desiccator for 1 hour. Lipids were resuspended in 400µL SUV Buffer (50mM HEPES,
711 100mM KCl, 1mM EDTA, 1mM $MgCl_2$, pH7.5) for 5mM lipid mixture stocks. The lipid
712 mixtures were vortexed until cloudy, and then transferred to 1.5mL Eppendorf tubes and
713 subjected to ten freeze-thaw cycles using a liquid nitrogen bath and 32˚C hot plate, with
714 2 minutes of sonication in a sonicating water bath following each thaw cycle. Stocks were
715 stored at -80˚C in 20µL aliquots.
716
717 Supported lipid bilayers were made by adding 10µL of SUVs to RCA cleaned
718 custom microwells built on 22x40mm #1.5 coverslips. Chambers were then incubated at
719 37°C for one hour to induce vesicle fusion, and unincorporated vesicles were rinsed away

using five rinses with 100μL SUV buffer. Yeast extract was added to these chambers by removing 90μL of buffer, leaving just enough to cover the chamber bottom, and then adding extract.

Statistics and Line Fitting

All plotting and statistical analysis was performed using GraphPad Prism 8.0.2(263) (GraphPad Software, San Diego, CA), except for MSD analysis, which was performed using MATLAB as described above. Analysis of statistical significance was performed using unpaired Student's T-tests for comparison of two data sets where appropriate or using single-factor ANOVA with Tukey's multiple comparison test for comparison of >2 data sets. The specific test used for each experiment and the results of that test are listed in the figure legends, with one exception: Analysis of the data presented in **Figure 3C,D** is provided in an ANOVA table in **Figure 3—figure supplement 1.**

In general, line fitting was performed using linear regression by least-squares with analysis of residuals to ensure fit. Where linear regression did not fit the biological question, we compared of multiple models (linear regression vs non-linear regression, and the coefficient of determination (R^2) was considered to determine best-fit. When considering the regression model in **Figure 6C,D**, visualization of the non-log scale plots revealed unambiguous exponential relationships between glucose concentration and the concentration of either Pom1 or Cdr2, reflecting saturable binding. In **Figure 7B,C**, insets indicate whether the slopes (b_1) and Y-intercepts (b_0) of the two linear regressions are significantly different at the 95% confidence level. Details of the linear regressions presented in **Figure 7B,C** and **Figure 7—figure supplement 1A,B** are provided in **Supplemental Table 1** and **Supplemental Table 2**. To summarize the results of a given test, statistical significance is indicated within plots by the convention: (****) indicates $p < 0.0001$, (***) indicates $p < 0.001$, (**) indicates $p < 0.01$, (*) indicates $p < 0.05$, n.s. indicated $p > 0.05$.

751 # Figure Legends:

752

753 Figure 1: **The Pom1 gradient is formed by time-averaging of clusters that transiently**
754 **bind the cortex. (A)** Schematic of the Cdr2-Pom1-Wee1 signal transduction pathway
755 and its coarse cellular localization. **(B)** Individual frame (top panel) and sum projection
756 (bottom panel) of a high-speed TIRF microscopy movie. Movie was continuous 15s time-
757 lapse acquisition of 200ms exposures. Scale bar 1µm. Blue arrows mark position of line
758 scans performed for data in panel (D). **(C)** Pom1-mNG also forms clusters at the cell tip.
759 Image is a sum projection of three consecutive 200ms exposures from continuous time-
760 lapse TIRF movie of the cell tip as depicted in the cartoon diagram. Scale bar 1µm. **(D)**
761 Line scans of fluorescence intensity along the long axis of the snap shot (blue line, left Y
762 axis) and projection images (red line, right Y axis) in panel (B). Note that time-averaging
763 of Pom1 clusters smoothens the concentration gradient. **(E)** Comparison of Pom1 cluster
764 binding frequency at the cell tip or side (****, p=<0.0001, n=10 cells, 42-170 traces/cell).
765 **(F)** Comparison of cortical dwell time of individual Pom1-mNG clusters (n.s., p=0.6747,
766 n=10 cells, 42-170 traces/cell) at the cell tip or side. For (E-F), each data point represents
767 a single cell mean, and line and error bars represent mean and standard deviation of all
768 cells. Statistical significance was tested using a Student's T-test.

769

770 Figure 1—figure supplement 1: **Analysis of the Pom1 gradient by confocal**
771 **microscopy**. **(A)** Pom1-mNG clusters are apparent at the lateral cell cortex of cells in
772 individual frames (200ms) of spinning-disc microscopy movies (top panel) but become
773 averaged out in a projection of the entire movie (bottom panel). Sum projection is of a
774 continuous 15s time-lapse acquisition of 200ms exposures at the top cell focal plane.
775 Scale bar 1µm. **(B)** Line scans of fluorescence intensity along the long axis of the cell in
776 the snap shot (blue line, left Y axis) and projection image (red line, right Y axis) at
777 positions marked by blue arrow heads in panel (A). Note that time-averaging of Pom1
778 clusters smoothens the concentration gradient. **(C)** Representative images of Airyscan
779 super-resolution micrographs of Pom1-mNG at cell tip or side. Scale bar, 1µm. **(D)**
780 Fluorescence intensities of all single clusters resolved in Airyscan images as in panel (C).
781 Data points represent individual cluster values, error bars are the mean and standard

782 deviation (*n*=87 tip, 158 side). **(E)** Histogram of the fluorescence intensity of individual
783 Pom1 clusters at the cell tip and cell side. Clusters were binned by fluorescence intensity
784 and displayed as a population frequency (*n*=48 tip, 158 side).
785
786 Figure 1—figure supplement 2: **Analysis of Pom1 cluster diffusion (A)** Pom1-mNG
787 clusters positioned at the cell middle, in a 2x2μm ROI as used for particle tracking. **(B)**
788 Single-particle diffusion traces of Pom1-mNG clusters show limited lateral diffusion in
789 cells. **(C)** Mean squared displacement (MSD) curves calculated from traces of individual
790 Pom1-mNG cluster diffusion as in panel (B). **(D)** Mean MSD curves generated from
791 averaging of 439 single-particle traces, coming from 6 different cells. Linear regression
792 of the initial linear segment (red line) of the curve provides the diffusion coefficient
793 $D=0.134\pm0.017\mu m^2/s$. Black line represents the weighted mean of all traces, and grey
794 lines indicate standard deviation. **(E)** Average life-time displacement of individual clusters
795 (***, *p*=0.0002, *n*=10 cells, 42-170 traces/cell). Line and error represent mean and
796 standard deviation. Statistical significance was tested using a Student's T-test.
797
798 Figure 2: **Pom1 clusters are stable structures that can be isolated *in vitro.* (A)** TIRF
799 microscopy image of Pom1-mNG clusters in the extruded cytoplasm (white dotted line)
800 of a lysed cell (yellow dotted line). Scale bar 5μm. **(B)** TIRF microscopy images of cell
801 extracts prepared from wild-type (no tag) or Pom1-mNG cells. Images are 50 frame sum
802 projections of continuous 200ms time-lapse exposures. The two images were contrasted
803 equally. Scale bars 1μm. **(C)** Cytoplasmic extracts of *pom1-3HA* cells were subjected to
804 velocity sucrose gradient sedimentation, and fractions were probed against the HA tag
805 (upper blot). Fraction 1 corresponds to the top of the gradient and contains smaller
806 structures; fraction 9 corresponds to bottom of the gradient and contains larger structures.
807 Fractions 6-8 were pooled, sucrose was removed by dialysis, and then the sample was
808 subjected to a second identical round of sucrose gradient sedimentation and western
809 blotting of the resulting fractions (lower blot). **(D)** TIRF microscopy of Pom1-mNG clusters
810 from cytoplasmic extracts on supported lipid bilayers. Scale bar 1μm. Left panel is single
811 time point image. Right panel is kymograph taken from a line scan of time-lapse TIRF
812 experiment. **(E)** Quantification of binding duration of Pom1-mNG clusters on supported

813 lipid bilayers imaged by TIRF microscopy as in panel (D). Values are compared to cellular
814 measurements of Pom1 clusters on cell sides (n.s., p=0.05954, n= 713 *in vivo*, 421 *in*
815 *vitro*). **(F)** Quantification of life-time displacement of Pom1-mNG clusters diffusing on
816 supported lipid bilayers imaged by TIRF microscopy as in panel (D). Values are compared
817 to cellular measurements of Pom1 clusters on cell sides (****, p<0.0001, n= 713 *in vivo*,
818 421 *in vitro*). For (E) and (F), statistical significance was tested using a Student's T-test.
819 **(G)** Purified GST-Pom1 was subjected to sucrose gradient sedimentation and the
820 fractions were probed against the GST tag (upper blot). Purified GST-Pom1 was also
821 added to wild-type or *pom1*Δ cell extracts and incubated for 1hr at 4˚C in the presence of
822 ATP before velocity sucrose sedimentation and western blotting (bottom blots).
823
824 Figure 2—figure supplement 1: **Controls and supporting *in vitro* analysis of Pom1**
825 **clusters. (A)** Fluorescence intensity trace of a single Pom1-mNG cluster binding to the
826 cell cortex, measured by high speed TIRF microscopy (~50 frames per second with
827 continuous acquisition). Rapid intensity changes indicating binding and unbinding are
828 marked by green upward and magenta downward pointing arrows respectively. **(B)** FRAP
829 analysis of supported lipid bilayers. Upper panel: A circular ROI (teal dashed line) was
830 used to bleach fluorescent PE in the bilayers. Lower panel: Kymograph at white dashed
831 line in upper panel of fluorescence recovery as monitored by TIRF microscopy, indicating
832 fluidity. **(C)** Quantification and comparison of binding duration of either wild-type or
833 kinase-dead Pom1-mNG clusters to supported lipid bilayers in TIRF microscopy movies
834 (***p=<0.0001, n=1526 wild-type, 1993 kinase-dead). Statistical significance was tested
835 with a Student's T-test. **(D)** TIRF microscopy images of cell extracts prepared from cells
836 co-expressing Pom1-mNG and Cdr2-tagRFP-t. Pom1 clusters are shown in green and
837 Cdr2 nodes are shown in magenta. Images are 3 frame sum projections of continuous
838 200ms time-lapse exposures. Scale bar 1μm.
839
840 Figure 2—figure supplement 2: **Quantification of Pom1 sedimentation in velocity**
841 **sucrose gradients and size standards. (A)** Quantification of Pom1-3HA band
842 intensities from western blot of yeast extracts in main **(Figure 2C)**. **(B)** Size standards for
843 velocity sucrose gradients, as in main (Figure 2C,G). Data are quantified from single

844 Coomassie-stained gels or using spectrophotometry data. **(C)** Plot of S-value versus
845 sedimentation peak. Line is the linear regression of the three size standards, with the S-
846 value for Pom1 peaks interpolated.
847
848 Figure 2—figure supplement 3: **Analysis of Pom1 cluster diffusion on supported lipid**
849 **bilayers (A)** Pom1-mNG clusters diffusing on supported lipid bilayers imaged by high-
850 speed (100ms acquisition) TIRF microscopy. **(B)** Single-particle diffusion traces of Pom1-
851 mNG clusters on supported lipid bilayers. **(C)** Mean squared displacement (MSD) curves
852 calculated from traces of individual Pom1-mNG cluster diffusion as in panel (B). **(D)** Mean
853 MSD curves generated from averaging of 421 single-particle traces. Weighted linear
854 regression of the curve (red line) provides the diffusion coefficient D= 0.168±0.018μm^2/s.
855 Note that the weighted regression best fits the initial region of the curve because few
856 clusters bind longer than 10s. Black line represents weighted mean of all traces, grey
857 lines indicate standard deviation, and error bars represent weighted standard deviation.
858
859 Figure 3: **Polarity landmarks pattern cortical dynamics of Pom1 clusters to shape**
860 **the gradient. (A)** Western blots of sucrose gradient fractions after sedimentation analysis
861 as in Figure 2C of extracts prepared from *tea1*Δ or *tea4*Δ cells expressing Pom1-3HA. **(B)**
862 TIRF micrographs of Pom1-mNG localization at the tip or side cortex in *tea1*Δ or *tea4*Δ
863 cells. Scale bar 1μm. **(C)** The mean binding frequency of Pom1-mNG clusters at the tips
864 and sides of wild-type, *tea1*Δ or *tea4*Δ cells (*n*=10 cells, 7-170 traces/cell). **(D)** The mean
865 dwell time of Pom1-mNG clusters at the tips and sides of wild-type, *tea1*Δ or *tea4*Δ cells.
866 For panels C-D, wild-type data are replotted from main **(Figure 1)**. Each data point
867 represents a single cell mean, and line and error bars represent mean and standard
868 deviation of all cells (*n*=10 cells, 7-170 traces/cell). Comparisons are 1-way ANOVA with
869 Tukey's multiple comparisons tests. (****) indicates $p < 0.0001$, (n.s.) indicates $p > 0.05$.
870 See Figure 3—figure supplement 1D for all results of statistical analysis.
871
872 Figure 3—figure supplement 1: **Supporting analysis of Pom1 clusters in polarity**
873 **mutants. (A)** Confocal micrographs of Pom1-mNG in *tea1*Δ or *tea4*Δ cells. Images are
874 from the middle focal plane; scale bar 5μm. **(B)** Quantification of cortical binding dwell

875 time of individual Pom1-mNG clusters at the tips or sides of representative wild-type,
876 *tea1*Δ or *tea4*Δ cells (*n*=44-129 traces). **(C)** Quantification of total lifetime displacement of
877 individual Pom1-mNG clusters at the tips or sides of representative wild-type, *tea1*Δ or
878 *tea4*Δ cells. For B-C, line and error represent single cell mean and standard deviation
879 (*n*=44-129 traces). **(D)** Results of ANOVA and Tukey's multiple comparison tests
880 performed in main (Figure 3C,D).
881
882 Figure 4: **Size-scaling of Pom1 clusters and Cdr2 nodes at the lateral cell cortex. (A)**
883 A subset of Pom1 clusters colocalize with Cdr2 nodes. Panels are TIRF microscopy
884 images of cells expressing Pom1-mNG and Cdr2-tagRFP-t. Yellow dashed brackets
885 outline the ROI of the lower zoomed panels. Orange arrows point to Pom1 clusters
886 colocalized with Cdr2 nodes. Scale bar is 1μm**. (B)** Kymographs generated using the ROI
887 indicated in panel A. Cyan arrows indicate prominent Pom1 clusters, magenta arrows
888 indicate prominent Cdr2 nodes, and orange arrows indicate colocalization. **(C)**
889 Localization of Cdr2-mEGFP (upper panels) or Pom1-mNG (lower panels) in
890 representative cells of increasing size, imaged by TIRF microscopy. Scale bar is 1μm.
891 **(D)** Total number of Cdr2-mEGFP nodes (blue circles) or Pom1-mNG clusters (red
892 squares) measured per cell. Quantification is limited to clusters detected and resolvable
893 in the TIRF illumination field. The slopes of the corresponding linear regressions are not
894 significantly different (p=0.3757, n>40 cells). **(E)** Density of Cdr2-mEGFP nodes (blue
895 circles) or Pom1-mNG clusters (red squares) in 2x2μm square ROIs at the cell middle,
896 counted using TIRF microscopy. The slopes of the corresponding linear regressions are
897 significantly different (p<0.0001, n>40 cells). **(F)** Example of colocalization analysis for
898 Pom1 clusters (magenta ROI) and Cdr2 nodes (cyan ROI) (left panels). Colocalized
899 structures are marked with overlapping yellow ROIs, whereas non-colocalizing structures
900 are marked with grey ROIs (right panel, grey circles). **(G)** Ratio of free Cdr2 nodes to free
901 Pom1 clusters, plotted as a function of cell size. The slope of the linear regression is
902 positive and significantly non-zero (p=0.0002, R^2=0.33, n=36 cells).
903
904 Figure 4—figure supplement 1: **Quantification of Pom1 and Cdr2 concentration in**
905 **different cellular regions. (A)** Schematic showing the ROI locations used to measure

906 the concentration of Pom1-mNG or Cdr2-mNG in the cytoplasm, cortex, tip cortex, or side
907 cortex. Images are spinning disc confocal micrographs of middle cell focal planes. Scale
908 bars 1μm. **(B)** Quantification of Cdr2 concentration (average fluorescence per pixel) at
909 different cellular ROIs as in panel (A). Each dot represents a measurement from a
910 different cell, numbers and the line and error represent the mean and standard deviation.
911 **(C)** Quantification of Pom1 concentration (average fluorescence per pixel) at different
912 cellular ROIs as in panel A. Each dot represents a measurement from a different cell,
913 numbers and the line and error represent the mean and standard deviation. **(D)**
914 Quantification of the cytoplasmic concentration (average fluorescence per pixel) of Cdr2-
915 mNG as a function of cell length, using a cytoplasmic ROI as in panel (A). The slope of
916 the linear regression does not significantly deviate from zero ($b_1 \neq 0$, (n.s.) p=0.6449). Each
917 point indicates a measurement from a single cell. **(E)** Quantification of the cytoplasmic
918 concentration (average fluorescence) of Pom1-mNG as a function of cell length, using a
919 cytoplasmic ROI as in panel (A). The slope of the linear regression does not significantly
920 deviate from zero ($b_1 \neq 0$, (n.s.) p=0.4926). Each point indicates a measurement from a
921 single cell.
922
923 Figure 4—figure supplement 2: **Colocalization of Cdr2 nodes and Pom1 clusters**
924 **using alternative fluorophore pair. (A)** A subset of Pom1 clusters colocalize with Cdr2
925 nodes. Images are dual-channel simultaneously-acquired TIRF microscopy images of
926 cells expressing Pom1-tdTomato and Cdr2-mNeonGreen. Yellow dashed brackets
927 outline the ROI of the lower zoomed panels. White arrows point to Pom1 clusters
928 colocalized with Cdr2 nodes. Scale bar is 1μm**. (B)** Kymographs generated using the ROI
929 drawn on the merged image in panel A. Cyan arrows indicate prominent Cdr2 nodes,
930 magenta arrows indicate prominent Pom1 clusters, and orange arrows adjacent to the
931 merged kymograph indicate colocalization.
932
933 Figure 4—figure supplement 3: **Supporting analysis of Cdr2 nodes and Pom1 clusters**
934 **at the medial cell cortex. (A)** Comparison of Pom1 cluster binding frequency on the cell
935 sides of wild-type and *cdr2*Δ cells (n.s., p=0.1076, n>10 cells, 25-42 traces/cell). **(B)**
936 Comparison of Pom1 cluster binding duration on the cell sides of wild-type and *cdr2*Δ

937 cells (n.s., p=0.371, n>10 cells, 25-42 traces/cell). **(C)** Comparison of Pom1 cluster
938 displacement on the cell sides of wild-type and *cdr2*Δ cells (n.s., p=0.8191, n>10 cells,
939 25-42 traces/cell). In A-C, significance was tested using a Student's T-test. **(D)** Schematic
940 and quantification of Pom1 concentration at the lateral cell cortex measured by confocal
941 microscopy, using 2μm line scans at the cell middle from images such as Figure 4—figure
942 supplement 1A. The slope of the linear regression is negative, but not significantly non-
943 zero (p=0.2603, R^2=0.03, n=45 cells). **(E)** Plot of the number of colocalized structures as
944 a function of cell size. The slope of the linear regression is significantly non-zero
945 (p=0.0006, R^2=0.3, n=36 cells). **(F)** Plot of free, non-colocalized Cdr2 nodes (blue circles)
946 and free Pom1 clusters (red squares). The slope of the linear regression of #Pom1
947 clusters versus cell length is negative, and significantly non-zero (p=0.001, R^2=0.27, n=36
948 cells). The slope of the linear regression of #Cdr2 nodes versus cell length is positive,
949 and significantly non-zero (p=0.021, R^2=0.15, n=36 cells).
950
951 Figure 5: **Redistribution of Pom1 clusters to the lateral cortex disrupts Cdr2 nodes**
952 **during glucose restriction. (A)** Localization of Pom1-mNG in cells grown in either high
953 (2%) or low (0.03%) glucose media. Images were collected using TIRF microscopy. Scale
954 bar, 5μm. **(B)** Comparison of the binding frequency of Pom1 clusters at the lateral cell
955 cortex in cells grown under high and low glucose (***, p=0.0003, n=10 cells, 32-113
956 traces/cell). Statistical significance was tested using a Student's T-test. **(C)** Comparison
957 of the binding dwell time of Pom1 clusters at the lateral cell cortex in cells grown under
958 high and low glucose (n.s., p=0.6833, n=10 cells, 32-113 traces/cell). Statistical
959 significance was tested using a Student's T-test. **(D)** Localization of Cdr2-mNG in wild-
960 type or *pom1*Δ cells grown in either normal (2%) or low (0.03%) glucose media. Images
961 were collected using TIRF microscopy. Scale bar, 1μm. **(E)** Comparison of the
962 fluorescence intensity of individual Cdr2-mNG nodes in wild-type or *pom1*Δ cells grown
963 in either normal (2%) or low (0.03%) glucose media. Low glucose induces partial node
964 disassembly in wild-type cells (****, p<0.0001, n=92-169 nodes from >5 cells) but not in
965 *pom1*Δ cells (n.s., p=0.4015, n=113-156 nodes from >5 cells). Measurements were taken
966 from Airyscan Super-Resolution confocal micrographs. **(F)** Quantification and comparison
967 of the total number of Cdr2-mNG nodes visible in TIRF micrographs of wild-type or *pom1*Δ

968 cells grown in either normal (2%) or low (0.03%) glucose media. There is no significant
969 difference in any condition (p>0.05, n=28-33 cells). Statistical significance was tested
970 using a one-way ANOVA.
971
972 Figure 5—figure supplement 1: **Redistribution of Pom1 clusters to the lateral cortex**
973 **disrupts Cdr2 nodes during glucose restriction, supporting data. (A)** Analysis of
974 Pom1 and Cdr2 redistribution by spinning-disc confocal microscopy, as in (Kelkar and
975 Martin, 2015). Images are confocal micrographs of cells co-expressing Pom1-tdTomato
976 and Cdr2-mNG in high (2%) or low (0.03%) glucose media. Scale bar, 5μm. **(B)** Cortical
977 fluorescence intensity of Cdr2 and Pom1 was measured using line scans drawn around
978 the circumference of the representative cell marked with an arrowhead in the 2% glucose
979 portion of panel A. **(C)** Cortical fluorescence intensity of Cdr2 and Pom1 was measured
980 using line scans drawn around the circumference of the representative cell marked with
981 an arrowhead in the 0.03% glucose portion of panel A.
982
983 Figure 6: **Pom1 and Cdr2 concentrations at the lateral cell cortex depend on glucose**
984 **availability and are anti-correlated. (A-B)** Localization of Pom1-mNG (panel A) and
985 Cdr2-mNG (panel B) in confocal micrographs at middle cell focal planes. Regions where
986 line-scans were used to measure fluorescence intensity are marked at the tip and side
987 (orange lines). Scale bar, 1μm. **(C)** Concentration of Pom1 (red squares) or Cdr2 (blue
988 circles) at cell sides in a range of glucose concentrations, measured using 'Side ROI' as
989 in panels A and B (n>10 cells/concentration). **(D)** Concentration of Pom1 (red squares)
990 or Cdr2 (blue circles) at cell tips in a range of glucose concentrations, measured using
991 'Tip ROI' as in panels A and B (n>10 cells/concentration). **(E)** Correlation of Cdr2 vs Pom1
992 concentrations at cell sides in each glucose concentration from panel C. Concentrations
993 are anticorrelated across all tested media glucose concentrations (p=0.0006, Pearson r=-
994 0.9352, n=8 concentrations). **(F)** Correlation of Cdr2 vs Pom1 concentrations at cell tips
995 in each glucose concentration from panel D. Concentrations show weak anticorrelation
996 across the tested media glucose concentrations, but the correlation is not statistically
997 significant (p=0.09, Pearson r=-0.65, n=8 concentrations).
998

999 Figure 7: **Pom1 redistribution under glucose restriction disrupts Wee1 regulation at**
1000 **cortical nodes. (A)** Localization of Wee1-mNG in wild-type or *pom1*Δ cells grown in
1001 either high (2%) or low (0.03%) glucose media. Images were collected using TIRF
1002 microscopy. Scale bar, 5μm. **(B)** Quantification of Wee1 bursting kinetics in wild-type cells
1003 grown under high (2%, blue circles) and low (0.03%, red squares) glucose conditions.
1004 The top panel is a plot of the total number of Wee1 bursts as a function of cell length,
1005 counted in single time point TIRF micrographs. The middle panel is a plot of the frequency
1006 of Wee1 bursts as a function of cell length. The bottom panel is a plot of Wee1 burst
1007 duration as a function of cell length. **(C)** Quantification of Wee1 bursting kinetics in *pom1*Δ
1008 cells grown under normal (2%, green circles) and low (0.03%, magenta squares) glucose
1009 conditions, as in panel B. For (B-C), insets represent whether the best fit values of the
1010 slope (b_1) and/or Y-intercept (b_0) of the two linear regressions are different at the 95%
1011 confidence level. See Supplemental Table 1 and Supplemental Table 2 for parameters of
1012 linear regressions and full statistical comparisons. **(D)** Western blot of Wee1 in wild-type,
1013 *pom1*Δ, and *cdr2*Δ cells grown in high (2%) or low (0.03%) glucose media showing
1014 phosphorylation dependent band-shifts.
1015
1016 Figure 7—figure supplement 1: **Wee1 bursting in low glucose phenocopies a kinase-**
1017 **dead Cdr2 mutant. (A)** Plot of the frequency of Wee1 bursts as a function of cell length
1018 in wild-type cells grown in high glucose (blue circles) and low glucose (red squares), or
1019 kinase-dead *cdr2(E177A)* mutant cells grown in high glucose (green triangles). **(B)** Plot
1020 of Wee1 burst duration as a function of cell length in wild-type cells grown in low glucose
1021 (red squares) and kinase-dead *cdr2(E177A)* mutant cells grown in high glucose (green
1022 triangles). For (A-B), insets represent whether the best fit values of the slope (b_1) and/or
1023 Y-intercept (b_0) of the linear regressions are different at the 95% confidence level. See
1024 Supplemental Table 1 and Supplemental Table 2 for parameters of linear regressions
1025 and full statistical comparisons.
1026
1027 Figure 8: **A model for the glucose-modulated control of Wee1 bursting by Pom1 and**
1028 **Cdr2.** See text for discussion.
1029

1030 Supplemental Table 1: **Parameters of linear regressions in Figure 7B,C and Figure**
1031 **7—figure supplement 1A,B.** For each data set, the table includes: The slope of the
1032 linear regression (b_1) and its 95% confidence intervals; whether the slope of the linear
1033 regression significantly deviates from zero at the 95% confidence interval; the Y-intercept
1034 of the linear regression (b_0) and its 95% confidence intervals; the coefficient of
1035 determination of the linear regression (R^2); the *n* of the data set.
1036
1037 Supplemental Table 2: **Summary of the statistical comparisons of the linear**
1038 **regressions in Figure 7B,C and Figure 7—figure supplement 1A,B.** For each
1039 comparison, the table includes: Whether the slopes of the linear regressions (b_1) are
1040 significantly different from each other at the 95% confidence level; whether the Y-
1041 intercepts of the linear regressions (b_0) are significantly different from each other at the
1042 95% confidence level. If the slopes of the linear regressions differed significantly, the
1043 difference in Y-intercepts was not tested.
1044
1045 Video 1: **Pom1-mNG forms clusters that transiently bind the cell cortex.** TIRF
1046 microscopy of a cell expressing Pom1-mNG from the endogenous locus. Frames are
1047 200ms exposures from continuous acquisition. Scale bar is 1µm.
1048
1049 Video 2: **Pom1-mNG clusters on synthetic supported lipid bilayers.** TIRF microscopy
1050 of Pom1-mNG clusters in cytoplasmic extracts, binding and releasing artificial supported
1051 lipid bilayers composed of phosphatidylcholine and phosphatidylserine. Frames are
1052 200ms exposures with 200ms interval between consecutive frames. Scale bar is 1µm.
1053

1054 # Acknowledgements:

1055 We thank members of the Moseley lab and Erik Griffin for comments on the manuscript.
1056 B. Wickner, C. Barlowe and the Norris Cotton Cancer Center Molecular Interactions &
1057 Imaging Core at Dartmouth for sharing equipment. A. Lavanway, Z. Svindrych and the
1058 Life Sciences Light Microscopy Facility for assistance with microscopy. A. Orr for
1059 assistance with ultracentrifugation. Y. Wu for recombinant Pom1 proteins. This work was
1060 supported by grants from the American Cancer Society (RSG-15-140-01-CCG) and the

1061 NIH (R01 GM099774) to J.B.M; and an NIH Training Grant (T32GM008704) to C.A.H.A.
1062 Shared imaging resources were supported by grants from the NIH (1S10OD018046 and
1063 P20GM113132).
1064

1065 # References:

1066 Akamatsu, M., Berro, J., Pu, K.-M., Tebbs, I.R., and Pollard, T.D. (2014). Cytokinetic
1067 nodes in fission yeast arise from two distinct types of nodes that merge during interphase.
1068 J Cell Biol *204*, 977–988.
1069

1070 Akamatsu, M., Lin, Y., Bewersdorf, J., and Pollard, T.D. (2017). Analysis of interphase
1071 node proteins in fission yeast by quantitative and superresolution fluorescence
1072 microscopy. MBoC *28*, 3203–3214.
1073

1074 Alberghina, L., Höfer, T., and Vanoni, M. (2009). Molecular networks and system-level
1075 properties. J. Biotechnol. *144*, 224–233.
1076

1077 Aligue, R., Wu, L., and Russell, P. (1997). Regulation of Schizosaccharomyces pombe
1078 Wee1 Tyrosine Kinase. J. Biol. Chem. *272*, 13320–13325.
1079

1080 Allard, C.A.H., Opalko, H.E., Liu, K.-W., Medoh, U., and Moseley, J.B. (2018). Cell size–
1081 dependent regulation of Wee1 localization by Cdr2 cortical nodes. J Cell Biol *217*, 1589–
1082 1599.
1083

1084 Bähler, J., and Nurse, P. (2001). Fission yeast Pom1p kinase activity is cell cycle
1085 regulated and essential for cellular symmetry during growth and division. The EMBO
1086 Journal *20*, 1064–1073.
1087

1088 Bähler, J., and Pringle, J.R. (1998). Pom1p, a fission yeast protein kinase that provides
1089 positional information for both polarized growth and cytokinesis. Genes Dev *12*, 1356–
1090 1370.
1091

1092 Bähler, J., Wu, J.-Q., Longtine, M.S., Shah, N.G., Iii, A.M., Steever, A.B., Wach, A.,
1093 Philippsen, P., and Pringle, J.R. (1998). Heterologous modules for efficient and versatile
1094 PCR-based gene targeting in Schizosaccharomyces pombe. Yeast *14*, 943–951.
1095
1096 Bhatia, P., Hachet, O., Hersch, M., Rincon, S.A., Berthelot-Grosjean, M., Dalessi, S.,
1097 Basterra, L., Bergmann, S., Paoletti, A., and Martin, S.G. (2014). Distinct levels in Pom1
1098 gradients limit Cdr2 activity and localization to time and position division. Cell Cycle *13*,
1099 538–552.
1100
1101 Bray, D., Levin, M.D., and Morton-Firth, C.J. (1998). Receptor clustering as a cellular
1102 mechanism to control sensitivity. Nature *393*, 85–88.
1103
1104 Breeding, C.S., Hudson, J., Balasubramanian, M.K., Hemmingsen, S.M., Young, P.G.,
1105 and Gould, K.L. (1998). The cdr2(+) gene encodes a regulator of G2/M progression and
1106 cytokinesis in Schizosaccharomyces pombe. Mol. Biol. Cell *9*, 3399–3415.
1107
1108 Chang, F., and Martin, S.G. (2009). Shaping Fission Yeast with Microtubules. Cold Spring
1109 Harb Perspect Biol *1*, a001347.
1110
1111 Coleman, T.R., Tang, Z., and Dunphy, W.G. (1993). Negative regulation of the weel
1112 protein kinase by direct action of the nim1/cdr1 mitotic inducer. Cell *72*, 919–929.
1113
1114 Deng, L., and Moseley, J.B. (2013). Compartmentalized nodes control mitotic entry
1115 signaling in fission yeast. Mol. Biol. Cell *24*, 1872–1881.
1116
1117 Deng, L., Baldissard, S., Kettenbach, A.N., Gerber, S.A., and Moseley, J.B. (2014).
1118 Dueling kinases regulate cell size at division through the SAD kinase Cdr2. Curr. Biol. *24*,
1119 428–433.
1120

1121 Dickinson, D.J., Schwager, F., Pintard, L., Gotta, M., and Goldstein, B. (2017). A Single-
1122 Cell Biochemistry Approach Reveals PAR Complex Dynamics during Cell Polarization.
1123 Dev. Cell *42*, 416-434.e11.
1124
1125 Dodgson, J., Chessel, A., Yamamoto, M., Vaggi, F., Cox, S., Rosten, E., Albrecht, D.,
1126 Geymonat, M., Csikasz-Nagy, A., Sato, M., et al. (2013). Spatial segregation of polarity
1127 factors into distinct cortical clusters is required for cell polarity control. Nature
1128 Communications *4*, 1834.
1129
1130 Dolznig, H., Grebien, F., Sauer, T., Beug, H., and Müllner, E.W. (2004). Evidence for a
1131 size-sensing mechanism in animal cells. Nat. Cell Biol. *6*, 899–905.
1132
1133 Douglass, A.D., and Vale, R.D. (2005). Single-molecule microscopy reveals plasma
1134 membrane microdomains created by protein-protein networks that exclude or trap
1135 signaling molecules in T cells. Cell *121*, 937–950.
1136
1137 Duke, T.A., and Bray, D. (1999). Heightened sensitivity of a lattice of membrane
1138 receptors. Proc. Natl. Acad. Sci. U.S.A. *96*, 10104–10108.
1139
1140 Facchetti, G., Chang, F., and Howard, M. (2017). Controlling cell size through sizer
1141 mechanisms. Current Opinion in Systems Biology *5*, 86–92.
1142
1143 Facchetti, G., Knapp, B., Flor-Parra, I., Chang, F., and Howard, M. (2019).
1144 Reprogramming Cdr2-Dependent Geometry-Based Cell Size Control in Fission Yeast.
1145 Current Biology *29*, 350-358.e4.
1146
1147 Falke, J.J. (2002). Cooperativity between bacterial chemotaxis receptors. Proc. Natl.
1148 Acad. Sci. U.S.A. *99*, 6530–6532.
1149
1150 Fantes, P.A. (1977). Control of cell size and cycle time in Schizosaccharomyces pombe.
1151 J. Cell. Sci. *24*, 51–67.

1152

1153 Fantes, P., and Nurse, P. (1977). Control of cell size at division in fission yeast by a
1154 growth-modulated size control over nuclear division. Exp. Cell Res. *107*, 377–386.
1155

1156 Feilotter, H., Nurse, P., and Young, P.G. (1991). Genetic and Molecular Analysis of
1157 Cdr1/Nim1 in Schizosaccharomyces Pombe. Genetics *127*, 309–318.
1158

1159 Gautier, J., Solomon, M.J., Booher, R.N., Bazan, J.F., and Kirschner, M.W. (1991). cdc25
1160 is a specific tyrosine phosphatase that directly activates p34cdc2. Cell *67*, 197–211.
1161

1162 Ginzberg, M.B., Kafri, R., and Kirschner, M. (2015). Cell biology. On being the right (cell)
1163 size. Science *348*, 1245075.
1164

1165 Gould, K.L., and Nurse, P. (1989). Tyrosine phosphorylation of the fission yeast cdc2 +
1166 protein kinase regulates entry into mitosis. Nature *342*, 39.
1167

1168 Gronnier, J., Crowet, J.-M., Habenstein, B., Nasir, M.N., Bayle, V., Hosy, E., Platre, M.P.,
1169 Gouguet, P., Raffaele, S., Martinez, D., et al. (2017). Structural basis for plant plasma
1170 membrane protein dynamics and organization into functional nanodomains. Elife *6*.
1171

1172 Gu, Y., and Oliferenko, S. (2019). Cellular geometry scaling ensures robust division site
1173 positioning. Nat Commun *10*, 268.
1174

1175 Guzmán-Vendrell, M., Rincon, S.A., Dingli, F., Loew, D., and Paoletti, A. (2015).
1176 Molecular control of the Wee1 regulatory pathway by the SAD kinase Cdr2. J. Cell. Sci.
1177 *128*, 2842–2853.
1178

1179 Hachet, O., Berthelot-Grosjean, M., Kokkoris, K., Vincenzetti, V., Moosbrugger, J., and
1180 Martin, S.G. (2011). A phosphorylation cycle shapes gradients of the DYRK family kinase
1181 Pom1 at the plasma membrane. Cell *145*, 1116–1128.
1182

1183 Harashima, H., Dissmeyer, N., and Schnittger, A. (2013). Cell cycle control across the
1184 eukaryotic kingdom. Trends Cell Biol. *23*, 345–356.
1185
1186 Haupt, A., and Minc, N. (2017). Gradients of phosphatidylserine contribute to plasma
1187 membrane charge localization and cell polarity in fission yeast. Mol Biol Cell *28*, 210–220.
1188
1189 Hersch, M., Hachet, O., Dalessi, S., Ullal, P., Bhatia, P., Bergmann, S., and Martin, S.G.
1190 (2015). Pom1 gradient buffering through intermolecular auto-phosphorylation. Mol. Syst.
1191 Biol. *11*, 818.
1192
1193 Jorgensen, P., and Tyers, M. (2004). How Cells Coordinate Growth and Division. Current
1194 Biology *14*, R1014–R1027.
1195
1196 Kalay, Z., Fujiwara, T.K., and Kusumi, A. (2012). Confining domains lead to reaction
1197 bursts: reaction kinetics in the plasma membrane. PLoS ONE *7*, e32948.
1198
1199 Kanoh, J., and Russell, P. (1998). The Protein Kinase Cdr2, Related to Nim1/Cdr1 Mitotic
1200 Inducer, Regulates the Onset of Mitosis in Fission Yeast. Mol Biol Cell *9*, 3321–3334.
1201
1202 Keifenheim, D., Sun, X.-M., D'Souza, E., Ohira, M.J., Magner, M., Mayhew, M.B.,
1203 Marguerat, S., and Rhind, N. (2017). Size-Dependent Expression of the Mitotic Activator
1204 Cdc25 Suggests a Mechanism of Size Control in Fission Yeast. Curr. Biol. *27*, 1491-
1205 1497.e4.
1206
1207 Kelkar, M., and Martin, S.G. (2015). PKA antagonizes CLASP-dependent microtubule
1208 stabilization to re-localize Pom1 and buffer cell size upon glucose limitation. Nature
1209 Communications *6*, 8445.
1210
1211 Kettenbach, A.N., Deng, L., Wu, Y., Baldissard, S., Adamo, M.E., Gerber, S.A., and
1212 Moseley, J.B. (2015). Quantitative phosphoproteomics reveals pathways for coordination

1213 of cell growth and division by the conserved fission yeast kinase pom1. Mol. Cell
1214 Proteomics *14*, 1275–1287.
1215
1216 Knight, J.D., Lerner, M.G., Marcano-Velázquez, J.G., Pastor, R.W., and Falke, J.J.
1217 (2010). Single Molecule Diffusion of Membrane-Bound Proteins: Window into Lipid
1218 Contacts and Bilayer Dynamics. Biophys J *99*, 2879–2887.
1219
1220 Kumagai, A., and Dunphy, W.G. (1991). The cdc25 protein controls tyrosine
1221 dephosphorylation of the cdc2 protein in a cell-free system. Cell *64*, 903–914.
1222
1223 Lee, S., Lim, W.A., and Thorn, K.S. (2013). Improved blue, green, and red fluorescent
1224 protein tagging vectors for S. cerevisiae. PLoS ONE *8*, e67902.
1225
1226 Liu, W., Wang, H., and Xu, C. (2016). Antigen Receptor Nanoclusters: Small Units with
1227 Big Functions. Trends Immunol. *37*, 680–689.
1228
1229 Lloyd, A.C. (2013). The Regulation of Cell Size. Cell *154*, 1194–1205.
1230
1231 Lucena, R., Alcaide-Gavilán, M., Anastasia, S.D., and Kellogg, D.R. (2017). Wee1 and
1232 Cdc25 are controlled by conserved PP2A-dependent mechanisms in fission yeast. Cell
1233 Cycle *16*, 428–435.
1234
1235 Maity, P.C., Blount, A., Jumaa, H., Ronneberger, O., Lillemeier, B.F., and Reth, M. (2015).
1236 B cell antigen receptors of the IgM and IgD classes are clustered in different protein
1237 islands that are altered during B cell activation. Sci Signal *8*, ra93.
1238
1239 Makushok, T., Alves, P., Huisman, S.M., Kijowski, A.R., and Brunner, D. (2016). Sterol-
1240 Rich Membrane Domains Define Fission Yeast Cell Polarity. Cell *165*, 1182–1196.
1241
1242 Martin, S.G., and Berthelot-Grosjean, M. (2009). Polar gradients of the DYRK-family
1243 kinase Pom1 couple cell length with the cell cycle. Nature *459*, 852–856.

1244

1245 Masuda, H., Fong, C.S., Ohtsuki, C., Haraguchi, T., and Hiraoka, Y. (2011).
1246 Spatiotemporal regulations of Wee1 at the G2/M transition. Mol. Biol. Cell *22*, 555–569.
1247

1248 Moreno, S., Hayles, J., and Nurse, P. (1989). Regulation of p34cdc2 protein kinase during
1249 mitosis. Cell *58*, 361–372.
1250

1251 Moreno, S., Nurse, P., and Russell, P. (1990). Regulation of mitosis by cyclic
1252 accumulation of p80cdc25 mitotic inducer in fission yeast. Nature *344*, 549–552.
1253

1254 Moreno, S., Klar, A., and Nurse, P. (1991). Molecular genetic analysis of fission yeast
1255 Schizosaccharomyces pombe. Meth. Enzymol. *194*, 795–823.
1256

1257 Morrell, J.L., Nichols, C.B., and Gould, K.L. (2004). The GIN4 family kinase, Cdr2p, acts
1258 independently of septins in fission yeast. Journal of Cell Science *117*, 5293–5302.
1259

1260 Moseley, J.B., Mayeux, A., Paoletti, A., and Nurse, P. (2009). A spatial gradient
1261 coordinates cell size and mitotic entry in fission yeast. Nature *459*, 857–860.
1262

1263 Munro, E. (2017). Protein Clustering Shapes Polarity Protein Gradients. Dev. Cell *42*,
1264 309–311.
1265

1266 Neumann, F.R., and Nurse, P. (2007). Nuclear size control in fission yeast. J Cell Biol
1267 *179*, 593–600.
1268

1269 Opalko, H.E., and Moseley, J.B. (2017). Dynamic regulation of Cdr1 localization and
1270 phosphorylation during osmotic stress. J. Biol. Chem. jbc.M117.793034.
1271

1272 Pan, K.Z., Saunders, T.E., Flor-Parra, I., Howard, M., and Chang, F. (2014). Cortical
1273 regulation of cell size by a sizer cdr2p. ELife *3*.
1274

1275 Parker, L.L., Walter, S.A., Young, P.G., and Piwnica-Worms, H. (1993). Phosphorylation
1276 and inactivation of the mitotic inhibitor Weel by the nim1/cdr1 kinase. Nature *363*, 736.
1277
1278 Pluskal, T., Hayashi, T., Saitoh, S., Fujisawa, A., and Yanagida, M. (2011). Specific
1279 biomarkers for stochastic division patterns and starvation-induced quiescence under
1280 limited glucose levels in fission yeast. FEBS J. *278*, 1299–1315.
1281
1282 Qian, H., Sheetz, M.P., and Elson, E.L. (1991). Single particle tracking. Analysis of
1283 diffusion and flow in two-dimensional systems. Biophysical Journal *60*, 910–921.
1284
1285 Rincon, S.A., Bhatia, P., Bicho, C., Guzman-Vendrell, M., Fraisier, V., Borek, W.E., Alves,
1286 F. de L., Dingli, F., Loew, D., Rappsilber, J., et al. (2014). Pom1 regulates the assembly
1287 of Cdr2–Mid1 cortical nodes for robust spatial control of cytokinesis. J Cell Biol *206*, 61–
1288 77.
1289
1290 Rodriguez, J., Peglion, F., Martin, J., Hubatsch, L., Reich, J., Hirani, N., Gubieda, A.G.,
1291 Roffey, J., Fernandes, A.R., St Johnston, D., et al. (2017). aPKC Cycles between
1292 Functionally Distinct PAR Protein Assemblies to Drive Cell Polarity. Dev. Cell *42*, 400-
1293 415.e9.
1294
1295 Russell, P., and Nurse, P. (1986). cdc25+ functions as an inducer in the mitotic control of
1296 fission yeast. Cell *45*, 145–153.
1297
1298 Russell, P., and Nurse, P. (1987). Negative regulation of mitosis by wee1+, a gene
1299 encoding a protein kinase homolog. Cell *49*, 559–567.
1300
1301 Saunders, T.E., Pan, K.Z., Angel, A., Guan, Y., Shah, J.V., Howard, M., and Chang, F.
1302 (2012). Noise reduction in the intracellular pom1p gradient by a dynamic clustering
1303 mechanism. Dev. Cell *22*, 558–572.
1304

1305 Sbalzarini, I.F., and Koumoutsakos, P. (2005). Feature point tracking and trajectory
1306 analysis for video imaging in cell biology. J. Struct. Biol. *151*, 182–195.
1307
1308 Schmoller, K.M., Turner, J.J., Kõivomägi, M., and Skotheim, J.M. (2015). Dilution of the
1309 cell cycle inhibitor Whi5 controls budding-yeast cell size. Nature *526*, 268–272.
1310
1311 Shiozaki, K. (2009). Nutrition-Minded Cell Cycle. Sci. Signal. *2*, pe74–pe74.
1312
1313 Simanis, V., and Nurse, P. (1986). The cell cycle control gene cdc2+ of fission yeast
1314 encodes a protein kinase potentially regulated by phosphorylation. Cell *45*, 261–268.
1315
1316 Spira, F., Mueller, N.S., Beck, G., von Olshausen, P., Beig, J., and Wedlich-Söldner, R.
1317 (2012). Patchwork organization of the yeast plasma membrane into numerous coexisting
1318 domains. Nature Cell Biology *14*, 640–648.
1319
1320 Strausfeld, U., Labbé, J.C., Fesquet, D., Cavadore, J.C., Picard, A., Sadhu, K., Russell,
1321 P., and Dorée, M. (1991). Dephosphorylation and activation of a p34cdc2/cyclin B
1322 complex in vitro by human CDC25 protein. Nature *351*, 242–245.
1323
1324 Su, X., Ditlev, J.A., Hui, E., Xing, W., Banjade, S., Okrut, J., King, D.S., Taunton, J.,
1325 Rosen, M.K., and Vale, R.D. (2016). Phase separation of signaling molecules promotes
1326 T cell receptor signal transduction. Science *352*, 595–599.
1327
1328 Tarantino, N., Tinevez, J.-Y., Crowell, E.F., Boisson, B., Henriques, R., Mhlanga, M.,
1329 Agou, F., Israël, A., and Laplantine, E. (2014). TNF and IL-1 exhibit distinct ubiquitin
1330 requirements for inducing NEMO–IKK supramolecular structures. J Cell Biol *204*, 231–
1331 245.
1332
1333 Tinevez, J.-Y., Perry, N., Schindelin, J., Hoopes, G.M., Reynolds, G.D., Laplantine, E.,
1334 Bednarek, S.Y., Shorte, S.L., and Eliceiri, K.W. (2017). TrackMate: An open and
1335 extensible platform for single-particle tracking. Methods *115*, 80–90.

1336

1337 Wang, S.-C., Low, T.Y.F., Nishimura, Y., Gole, L., Yu, W., and Motegi, F. (2017). Cortical
1338 forces and CDC-42 control clustering of PAR proteins for Caenorhabditis elegans
1339 embryonic polarization. Nat. Cell Biol. *19*, 988–995.

1340

1341 Weiß, K., Neef, A., Van, Q., Kramer, S., Gregor, I., and Enderlein, J. (2013). Quantifying
1342 the Diffusion of Membrane Proteins and Peptides in Black Lipid Membranes with 2-Focus
1343 Fluorescence Correlation Spectroscopy. Biophys J *105*, 455–462.

1344

1345 Wood, E., and Nurse, P. (2013). Pom1 and cell size homeostasis in fission yeast. Cell
1346 Cycle *12*, 3228–3236.

1347

1348 Wu, J.-Q., and Pollard, T.D. (2005). Counting cytokinesis proteins globally and locally in
1349 fission yeast. Science *310*, 310–314.

1350

1351 Wu, L., and Russell, P. (1993). Nim1 kinase promotes mitosis by inactivating Wee1
1352 tyrosine kinase. Nature *363*, 738–741.

1353

1354 Wu, L., Shiozaki, K., Aligue, R., and Russell, P. (1996). Spatial organization of the Nim1-
1355 Wee1-Cdc2 mitotic control network in Schizosaccharomyces pombe. Mol. Biol. Cell *7*,
1356 1749–1758.

1357

1358 Yanagida Mitsuhiro, Ikai Nobuyasu, Shimanuki Mizuki, and Sajiki Kenichi (2011). Nutrient
1359 limitations alter cell division control and chromosome segregation through growth-related
1360 kinases and phosphatases. Philosophical Transactions of the Royal Society B: Biological
1361 Sciences *366*, 3508–3520.

1362

1363 Young, P.G., and Fantes, P.A. (1987). Schizosaccharomyces pombe mutants affected in
1364 their division response to starvation. Journal of Cell Science *88*, 295–304.

1365

1366 Zhou, Y., and Hancock, J.F. (2015). Ras nanoclusters: Versatile lipid-based signaling
1367 platforms. Biochim. Biophys. Acta *1853*, 841–849.
1368

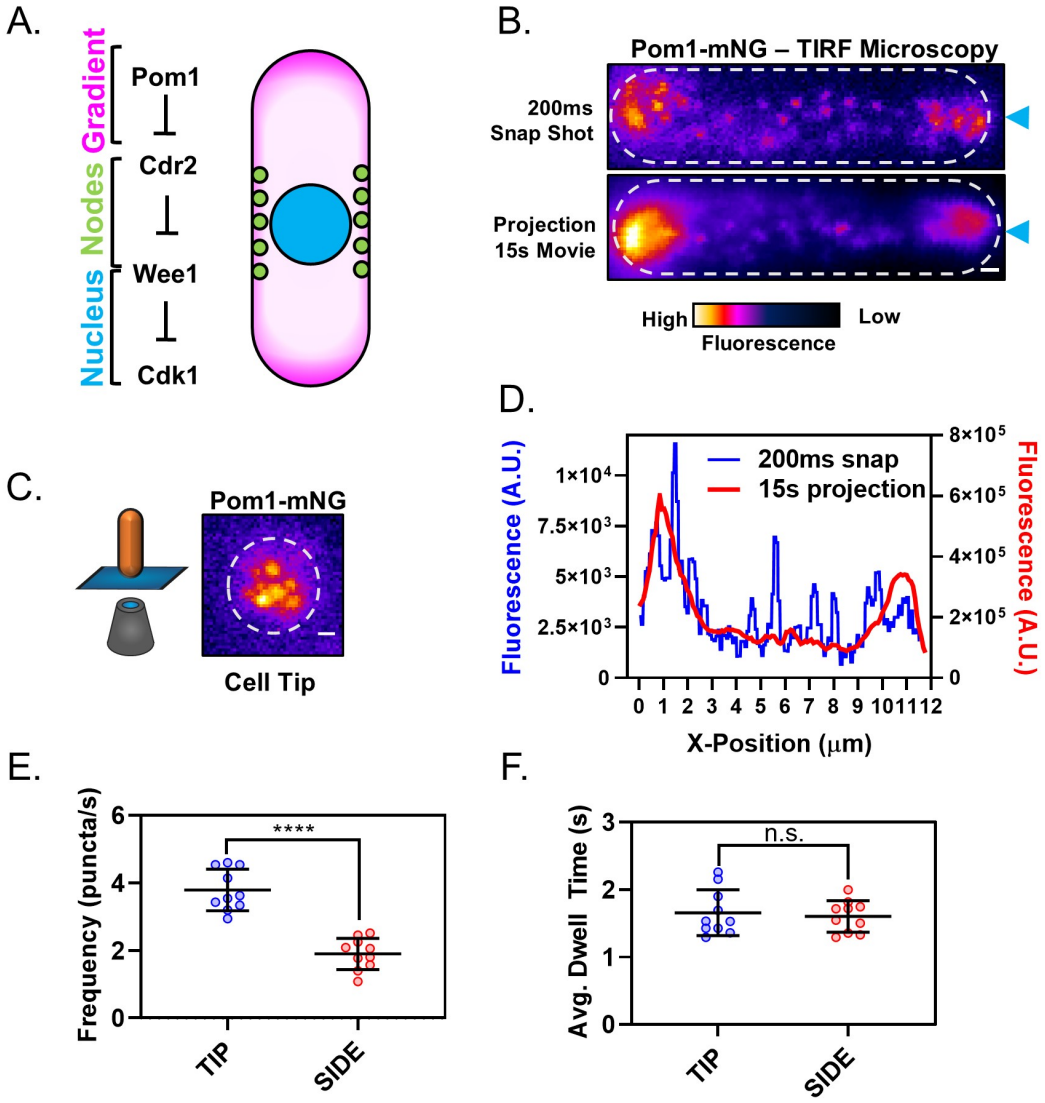
A.
Gradient
Nodes
Nucleus
Pom1
Cdr2
Wee1
Cdk1
B.
Pom1-mNG – TIRF Microscopy
200ms
Snap Shot
Projection
15s Movie
High
Low
Fluorescence
C.
Pom1-mNG
Cell Tip
D.
200ms snap
15s projection
Fluorescence (A.U.)
Fluorescence (A.U.)
X-Position (μm)
E.
Frequency (puncta/s)
****
TIP
SIDE
F.
Avg. Dwell Time (s)
n.s.
TIP
SIDE

Figure 1

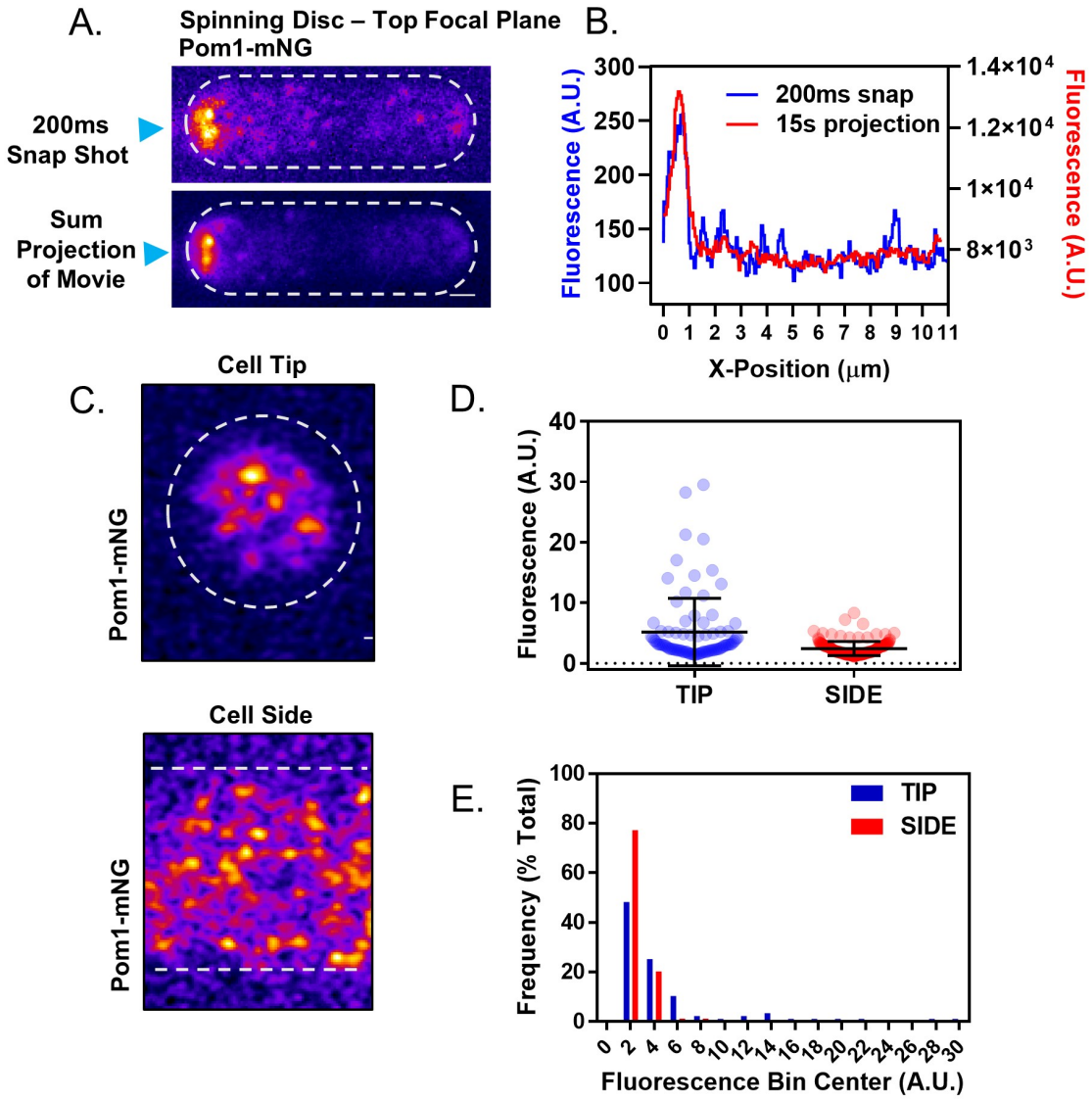

Figure 1 – figure supplement 1

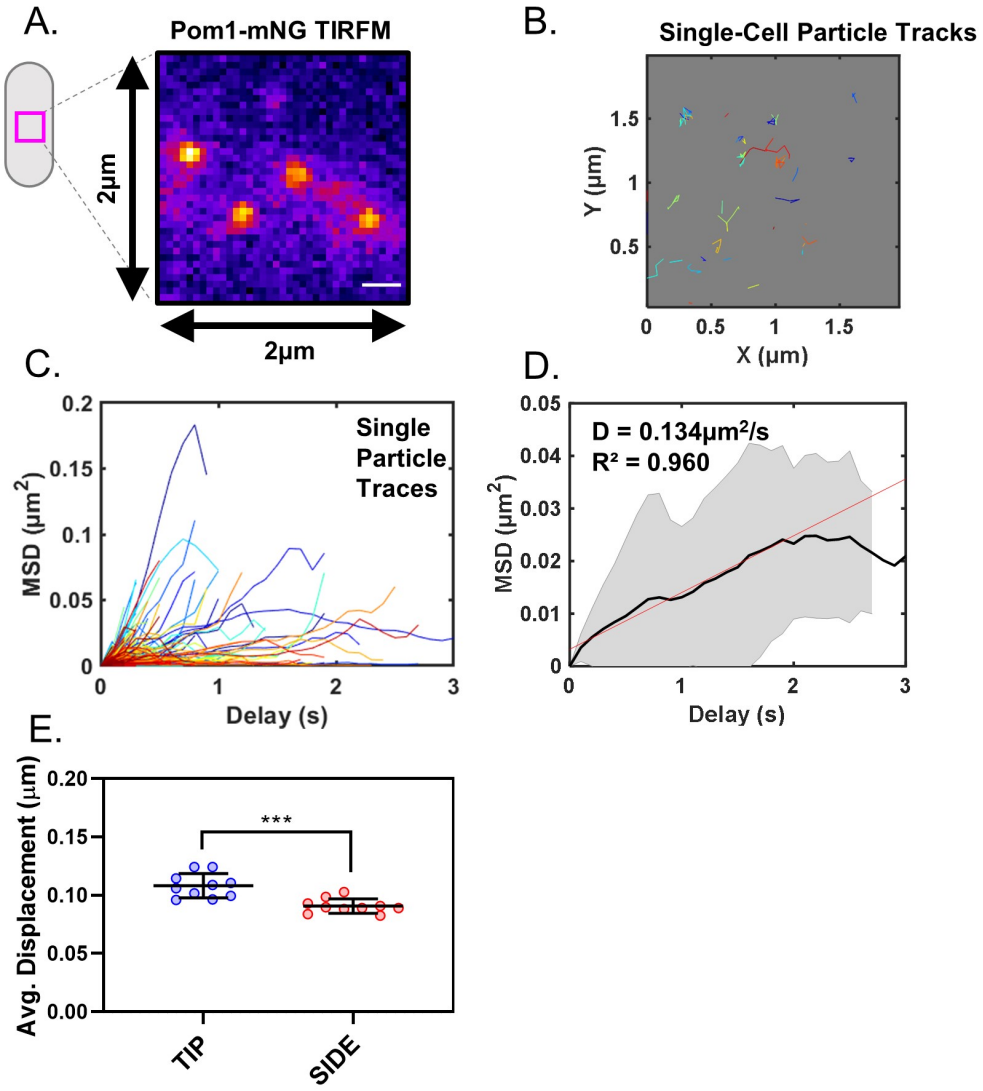

Figure 1 – figure supplement 2

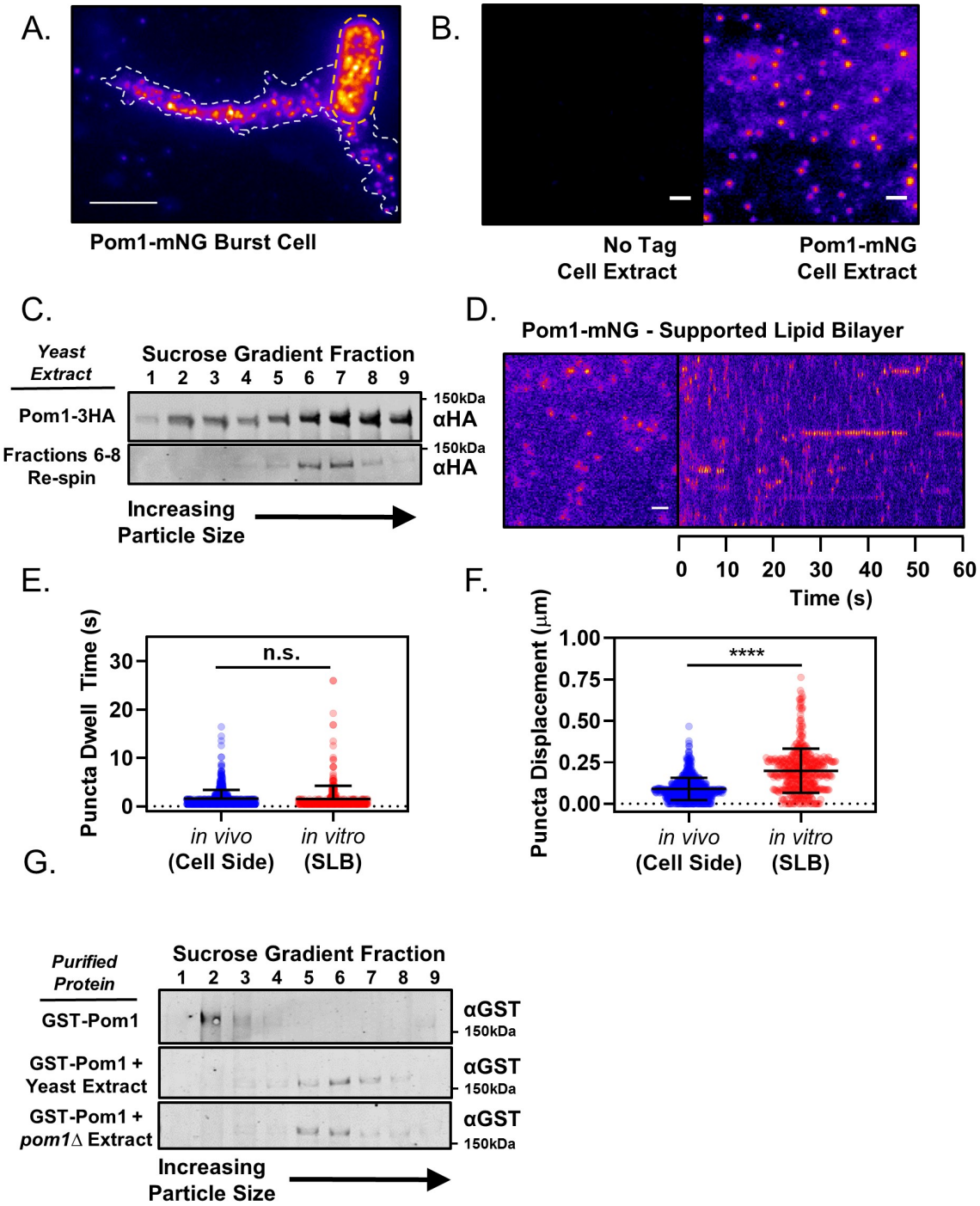
A.
Pom1-mNG Burst Cell
B.
No Tag
Cell Extract
Pom1-mNG
Cell Extract
C.
Yeast
Extract
Sucrose Gradient Fraction
1 2 3 4 5 6 7 8 9
Pom1-3HA
Fractions 6-8
Re-spin
150kDa
αHA
150kDa
αHA
Increasing
Particle Size
D.
Pom1-mNG - Supported Lipid Bilayer
0 10 20 30 40 50 60
Time (s)
E.
Puncta Dwell Time (s)
n.s.
30
20
10
0
in vivo
(Cell Side)
in vitro
(SLB)
F.
Puncta Displacement (μm)
****
1.00
0.75
0.50
0.25
0.00
in vivo
(Cell Side)
in vitro
(SLB)
G.
Purified
Protein
Sucrose Gradient Fraction
1 2 3 4 5 6 7 8 9
GST-Pom1
GST-Pom1 +
Yeast Extract
GST-Pom1 +
pom1Δ Extract
αGST
150kDa
αGST
150kDa
αGST
150kDa
Increasing
Particle Size

Figure 2

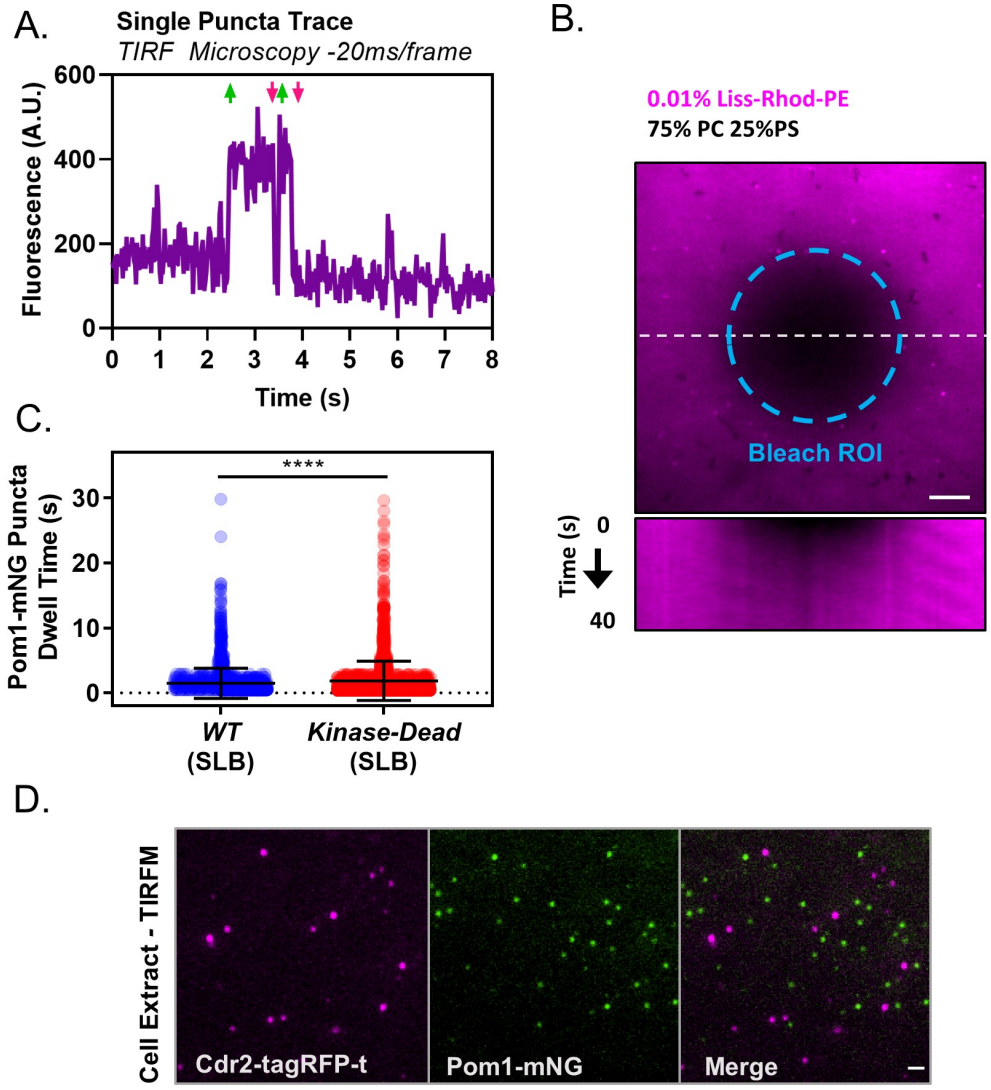

Figure 2 – figure supplement 1

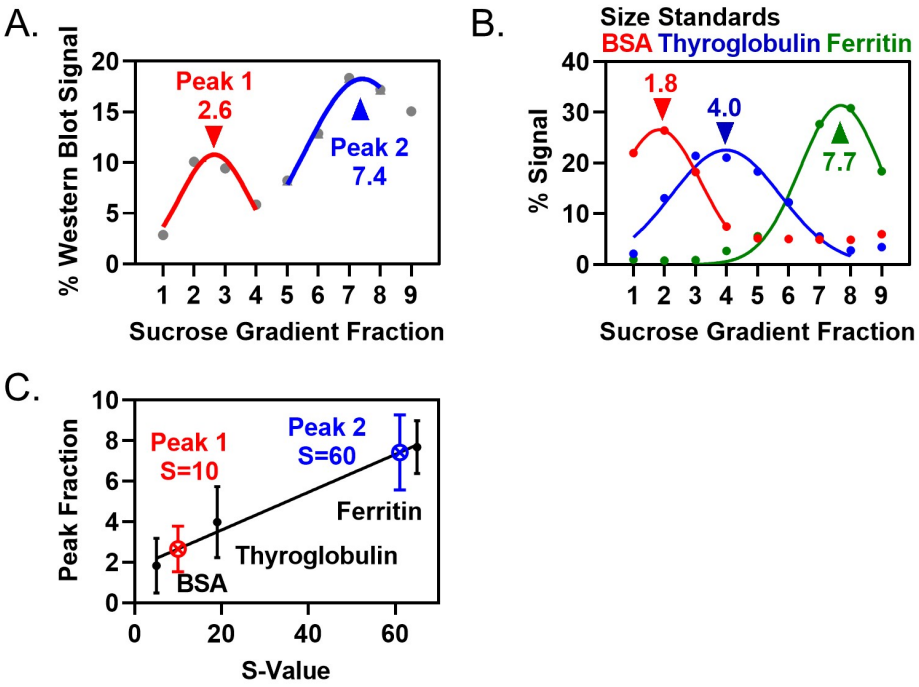

Figure 2 – figure supplement 2

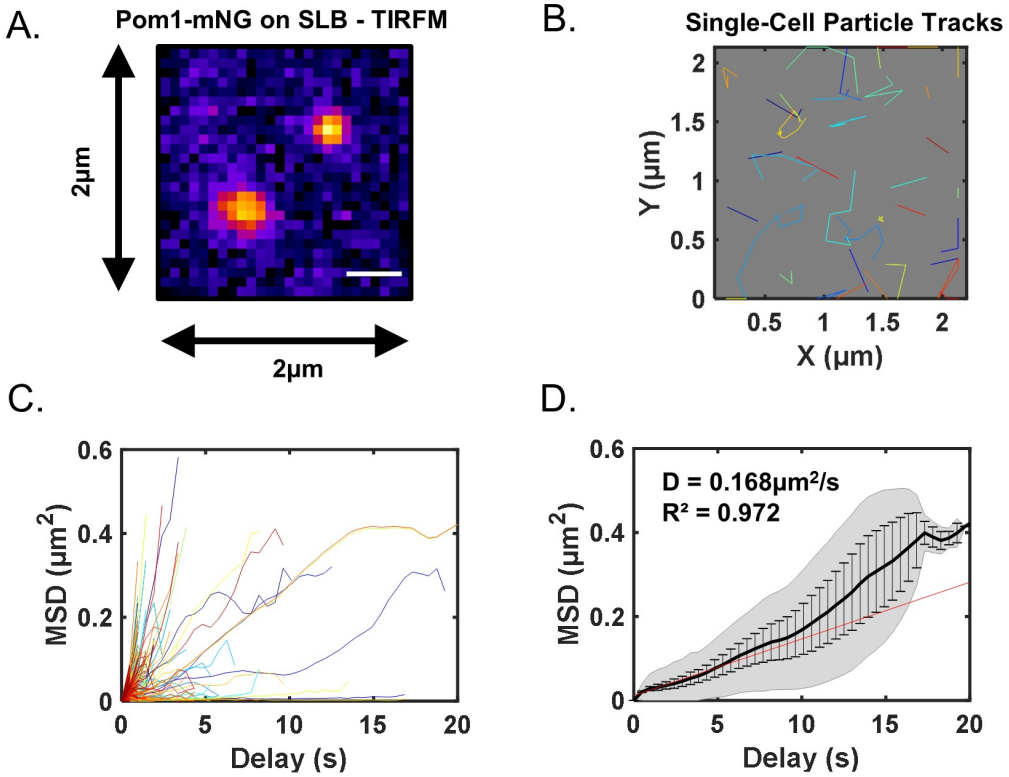

Figure 2 – figure supplement 3

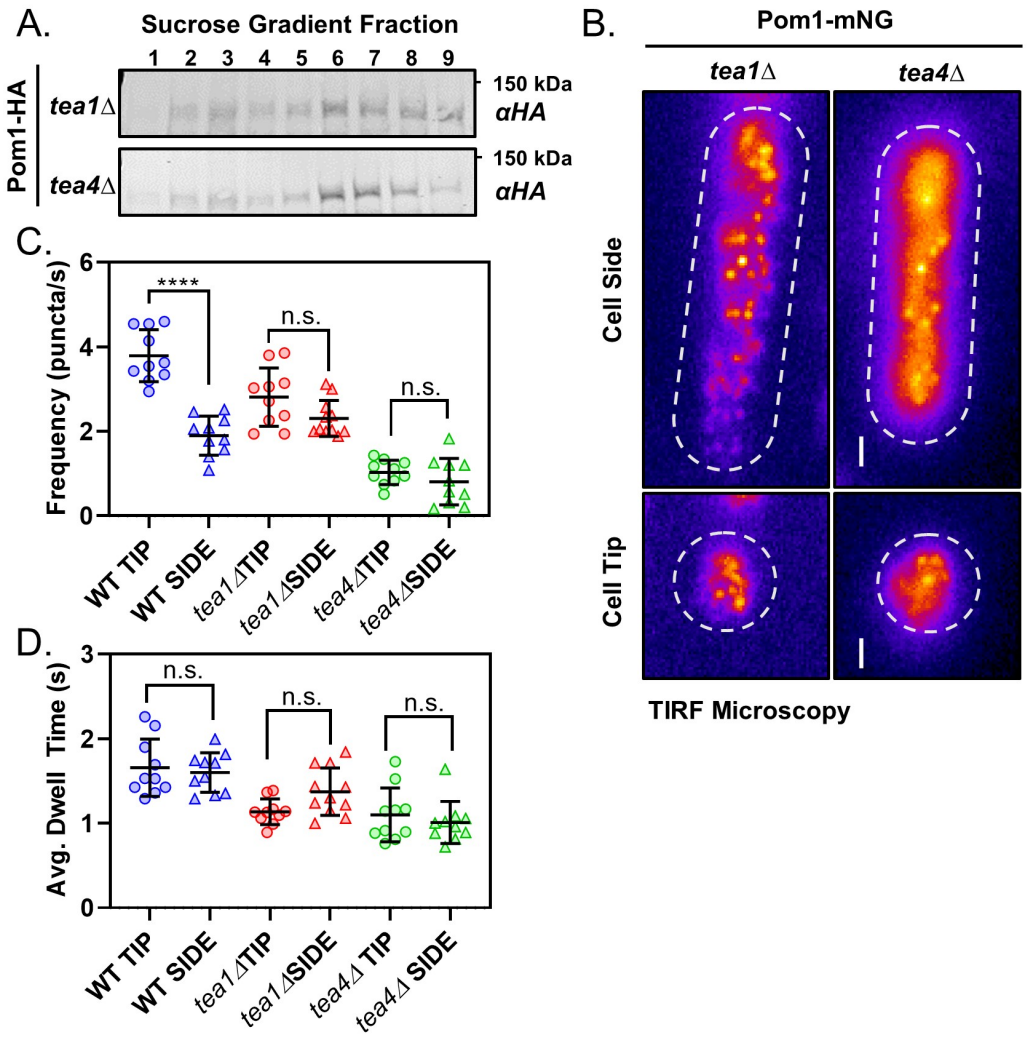
A.
Sucrose Gradient Fraction
1 2 3 4 5 6 7 8 9
Pom1-HA
tea1Δ
tea4Δ
150 kDa
αHA
150 kDa
αHA
B.
Pom1-mNG
tea1Δ
tea4Δ
Cell Side
Cell Tip
TIRF Microscopy
C.
Frequency (puncta/s)
****
n.s.
n.s.
WT TIP
WT SIDE
tea1ΔTIP
tea1ΔSIDE
tea4ΔTIP
tea4ΔSIDE
D.
Avg. Dwell Time (s)
n.s.
n.s.
n.s.
WT TIP
WT SIDE
tea1ΔTIP
tea1ΔSIDE
tea4Δ TIP
tea4Δ SIDE

Figure 3

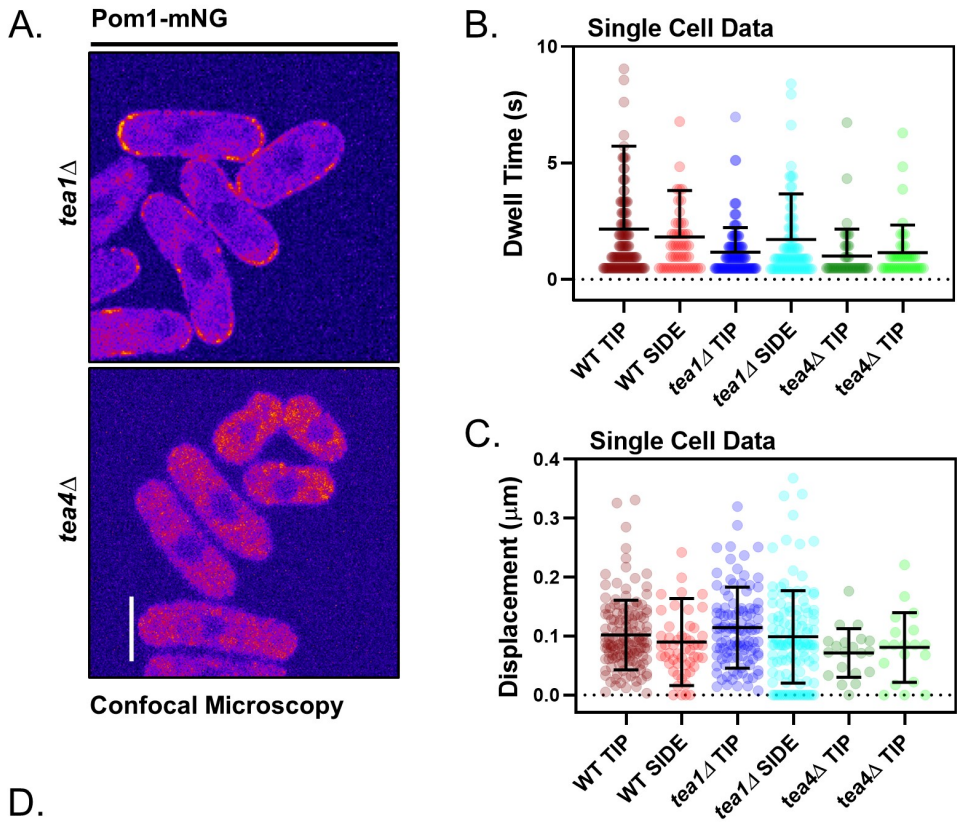

D.

ANOVA summary of **FREQUENCY**	
F	46.32
P value	<0.0001
P value summary	****
Significant diff. among means (P < 0.05)?	Yes
R square	0.8081

ANOVA summary of **DWELL TIME**	
F	10.34
P value	<0.0001
P value summary	****
Significant diff. among means (P < 0.05)?	Yes
R square	0.4846

	Tukey's Multiple Comparisons Summary of **FREQUENCY**				Tukey's Multiple Comparisons Summary of **DWELL TIME**			
-	Mean Diff.	Significant?	Summary	Adjusted P Value	Mean Diff.	Significant?	Summary	Adjusted P Value
WT TIP vs. WT SIDE	1.891	Yes	****	<0.0001	0.05557	No	ns	0.9972
WT TIP vs. tea1Δ TIP	0.98	Yes	**	0.0013	0.5207	Yes	***	0.0009
WT TIP vs. tea1Δ SIDE	1.485	Yes	****	<0.0001	0.2832	No	ns	0.1718
WT TIP vs. tea4Δ TIP	2.763	Yes	****	<0.0001	0.5577	Yes	***	0.0003
WT TIP vs. tea4Δ SIDE	2.983	Yes	****	<0.0001	0.6484	Yes	****	<0.0001
WT SIDE vs. tea1Δ TIP	-0.9114	Yes	**	0.0032	0.4651	Yes	**	0.0039
WT SIDE vs. tea1Δ SIDE	-0.4065	No	ns	0.4816	0.2277	No	ns	0.3927
WT SIDE vs. tea4Δ TIP	0.8714	Yes	**	0.0055	0.5022	Yes	**	0.0015
WT SIDE vs. tea4Δ SIDE	1.091	Yes	***	0.0003	0.5929	Yes	***	0.0001
tea1Δ TIP vs. tea1Δ SIDE	0.5049	No	ns	0.2449	-0.2375	No	ns	0.3458
tea1Δ TIP vs. tea4Δ TIP	1.783	Yes	****	<0.0001	0.03705	No	ns	0.9996
tea1Δ TIP vs. tea4Δ SIDE	2.003	Yes	****	<0.0001	0.1277	No	ns	0.8947
tea1Δ SIDE vs. tea4Δ TIP	1.278	Yes	****	<0.0001	0.2745	No	ns	0.1989
tea1Δ SIDE vs. tea4Δ SIDE	1.498	Yes	****	<0.0001	0.3652	Yes	*	0.034
tea4Δ TIP vs. tea4Δ SIDE	0.22	No	ns	0.9327	0.09068	No	ns	0.9741

Figure 3 – figure supplement 1

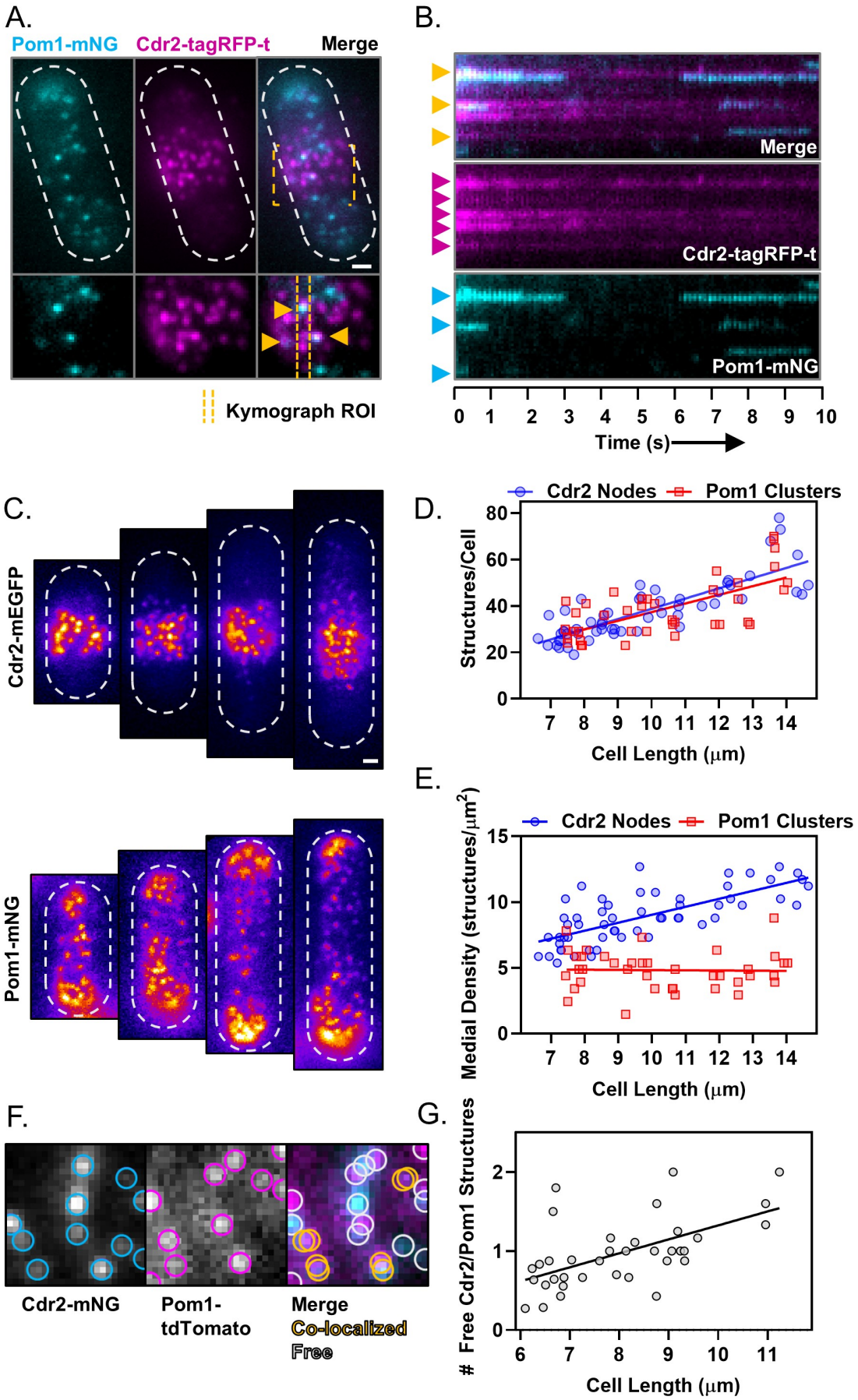
A.
Pom1-mNG
Cdr2-tagRFP-t
Merge
Kymograph ROI
B.
Merge
Cdr2-tagRFP-t
Pom1-mNG
0 1 2 3 4 5 6 7 8 9 10
Time (s)
C.
Cdr2-mEGFP
Pom1-mNG
D.
Cdr2 Nodes
Pom1 Clusters
Structures/Cell
0 20 40 60 80
7 8 9 10 11 12 13 14
Cell Length (μm)
E.
Cdr2 Nodes
Pom1 Clusters
Medial Density (structures/μm²)
0 5 10 15
7 8 9 10 11 12 13 14
Cell Length (μm)
F.
Cdr2-mNG
Pom1-tdTomato
Merge
Co-localized
Free
G.
Free Cdr2/Pom1 Structures
0 1 2
6 7 8 9 10 11
Cell Length (μm)

Figure 4

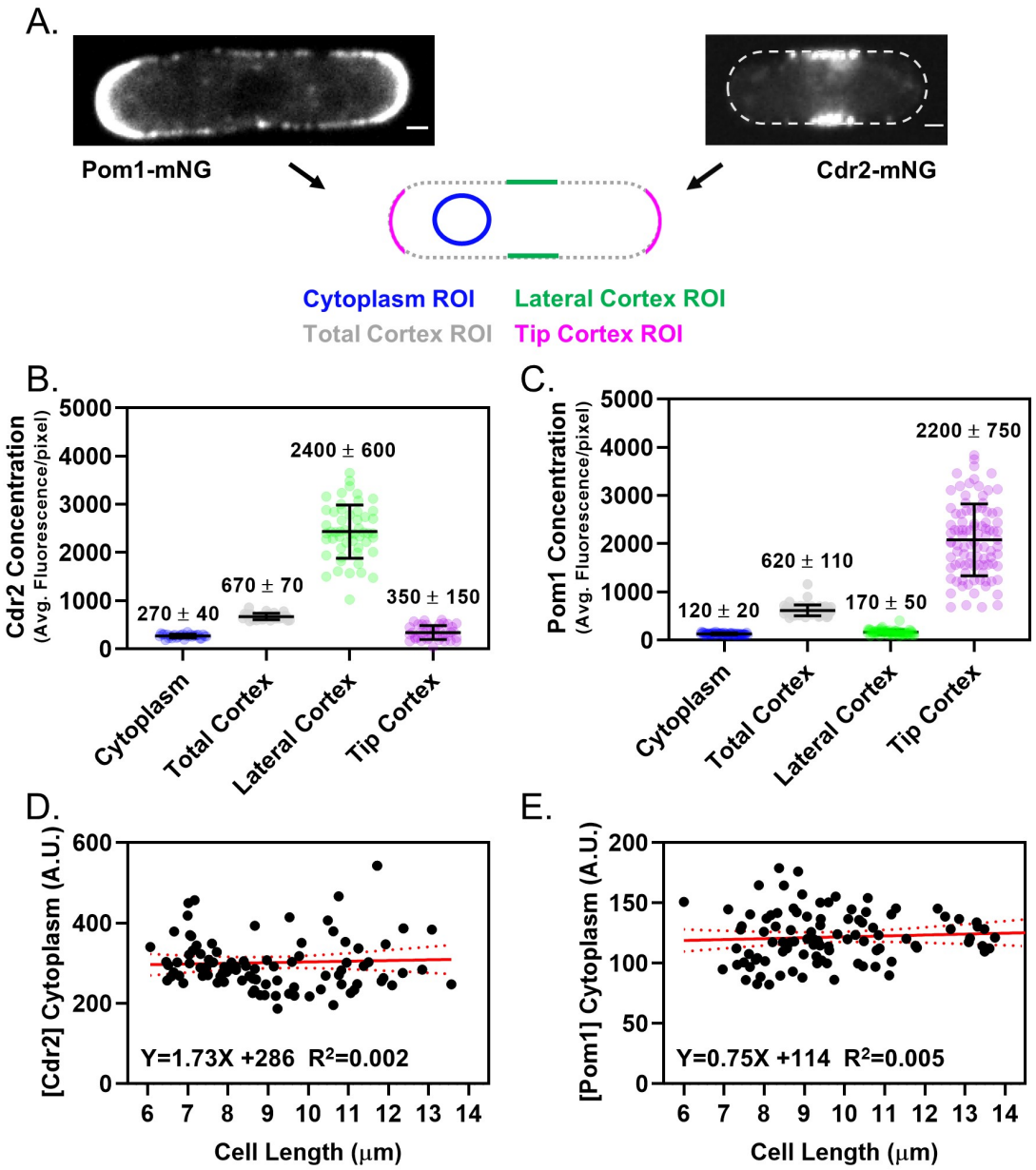

Figure 4 – figure supplement 1

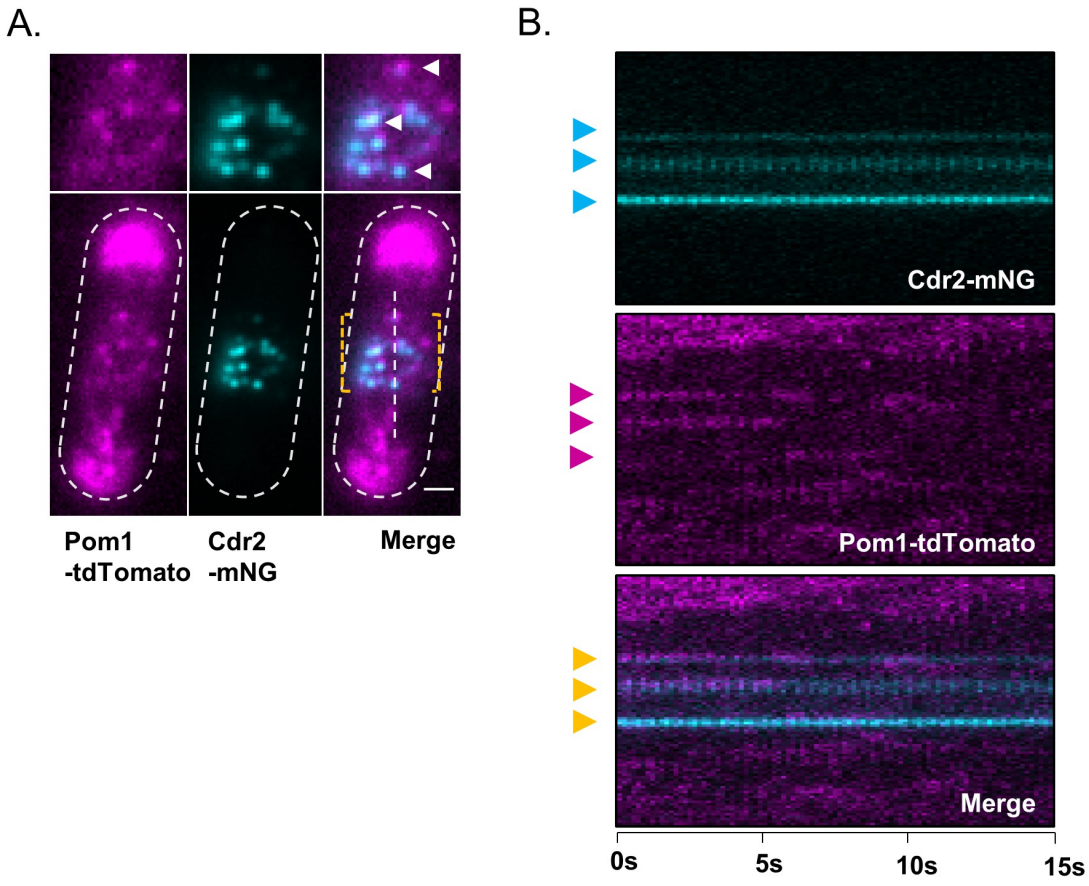

Figure 4 – figure supplement 2

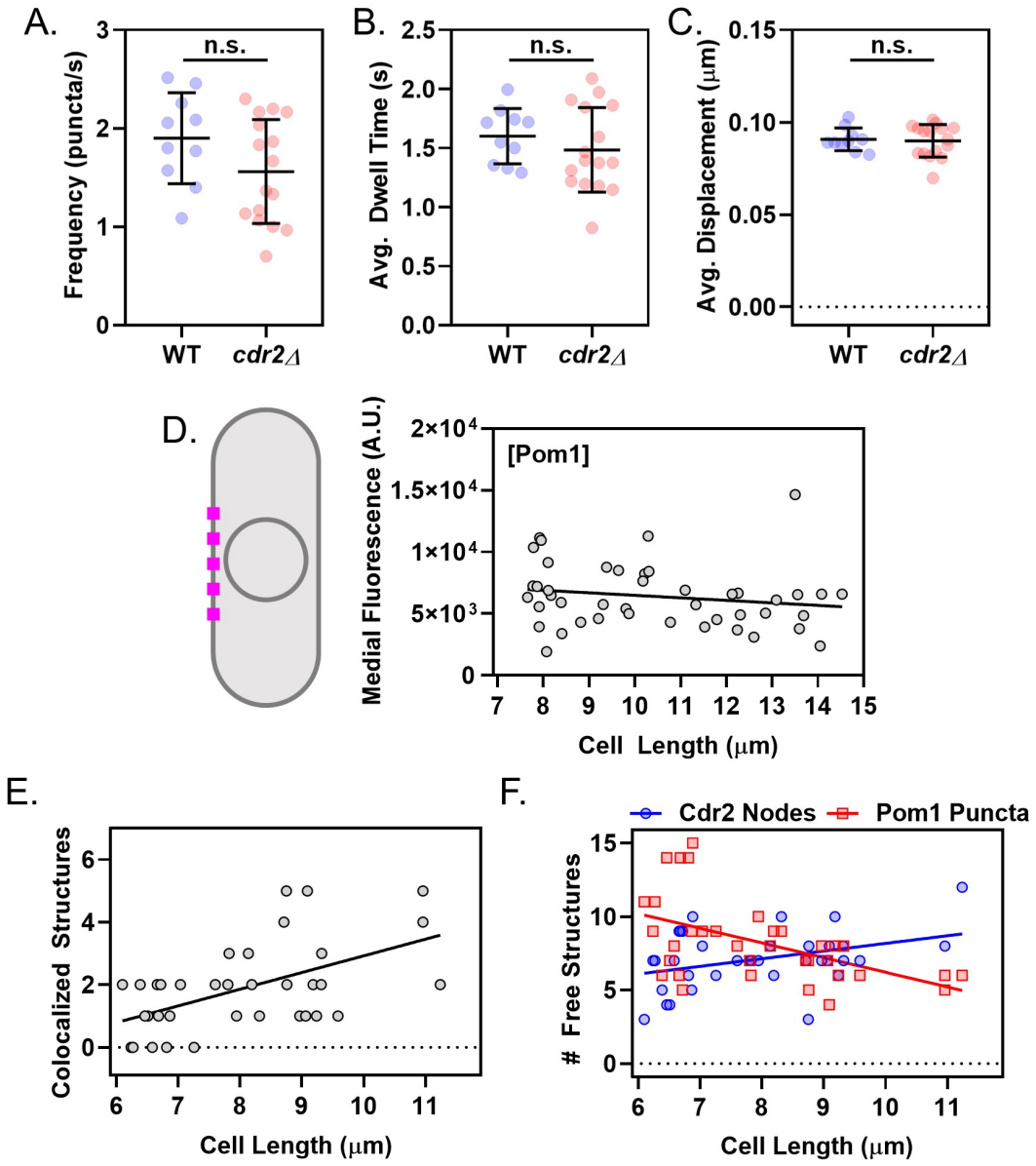

Figure 4 – figure supplement 3

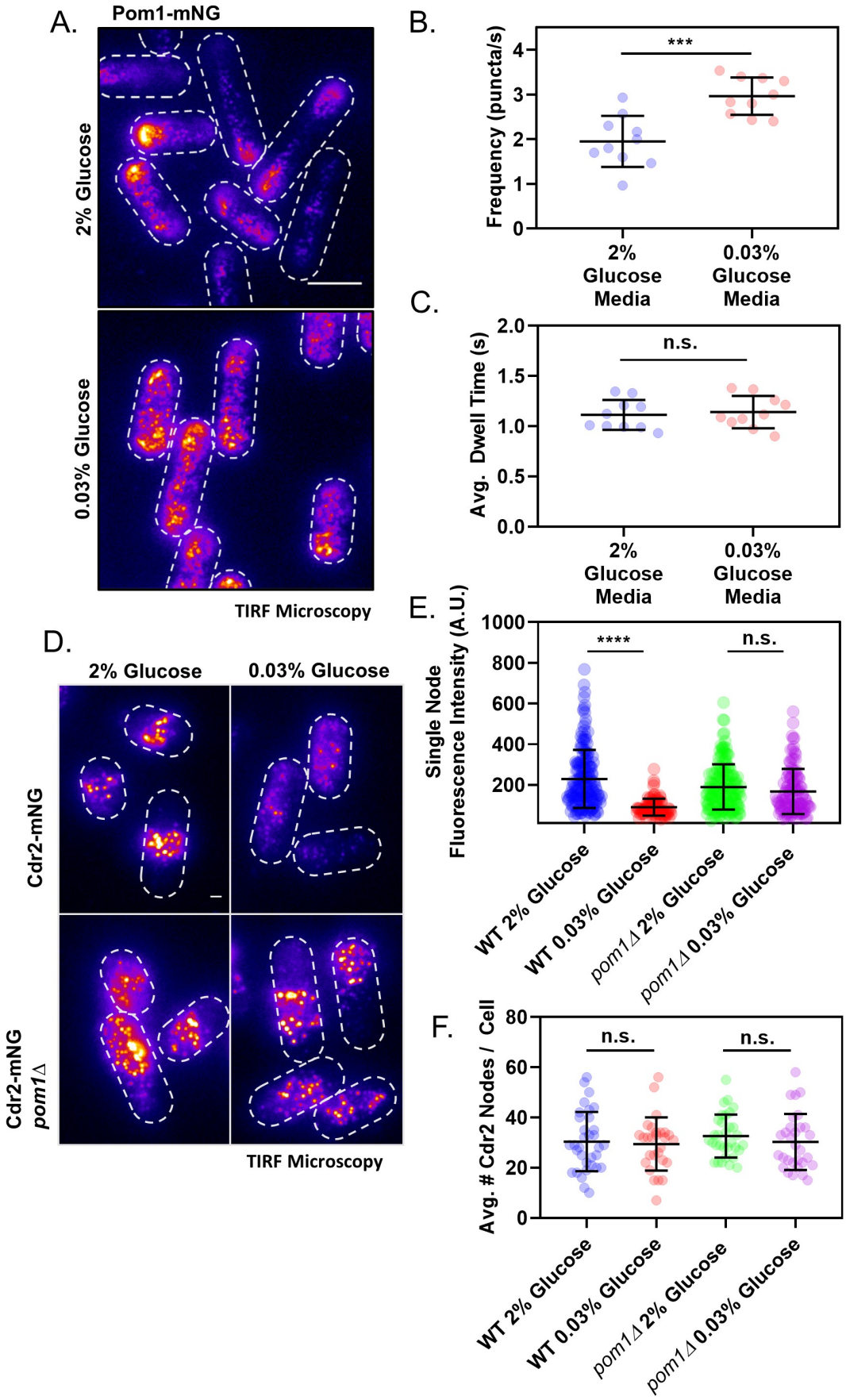
A.
Pom1-mNG
2% Glucose
0.03% Glucose
TIRF Microscopy
B.
Frequency (puncta/s)
***
2% Glucose Media
0.03% Glucose Media
C.
Avg. Dwell Time (s)
n.s.
2% Glucose Media
0.03% Glucose Media
D.
2% Glucose
0.03% Glucose
Cdr2-mNG
Cdr2-mNG pom1Δ
TIRF Microscopy
E.
Single Node Fluorescence Intensity (A.U.)
****
n.s.
WT 2% Glucose
WT 0.03% Glucose
pom1Δ 2% Glucose
pom1Δ 0.03% Glucose
F.
Avg. # Cdr2 Nodes / Cell
n.s.
n.s.
WT 2% Glucose
WT 0.03% Glucose
pom1Δ 2% Glucose
pom1Δ 0.03% Glucose

Figure 5

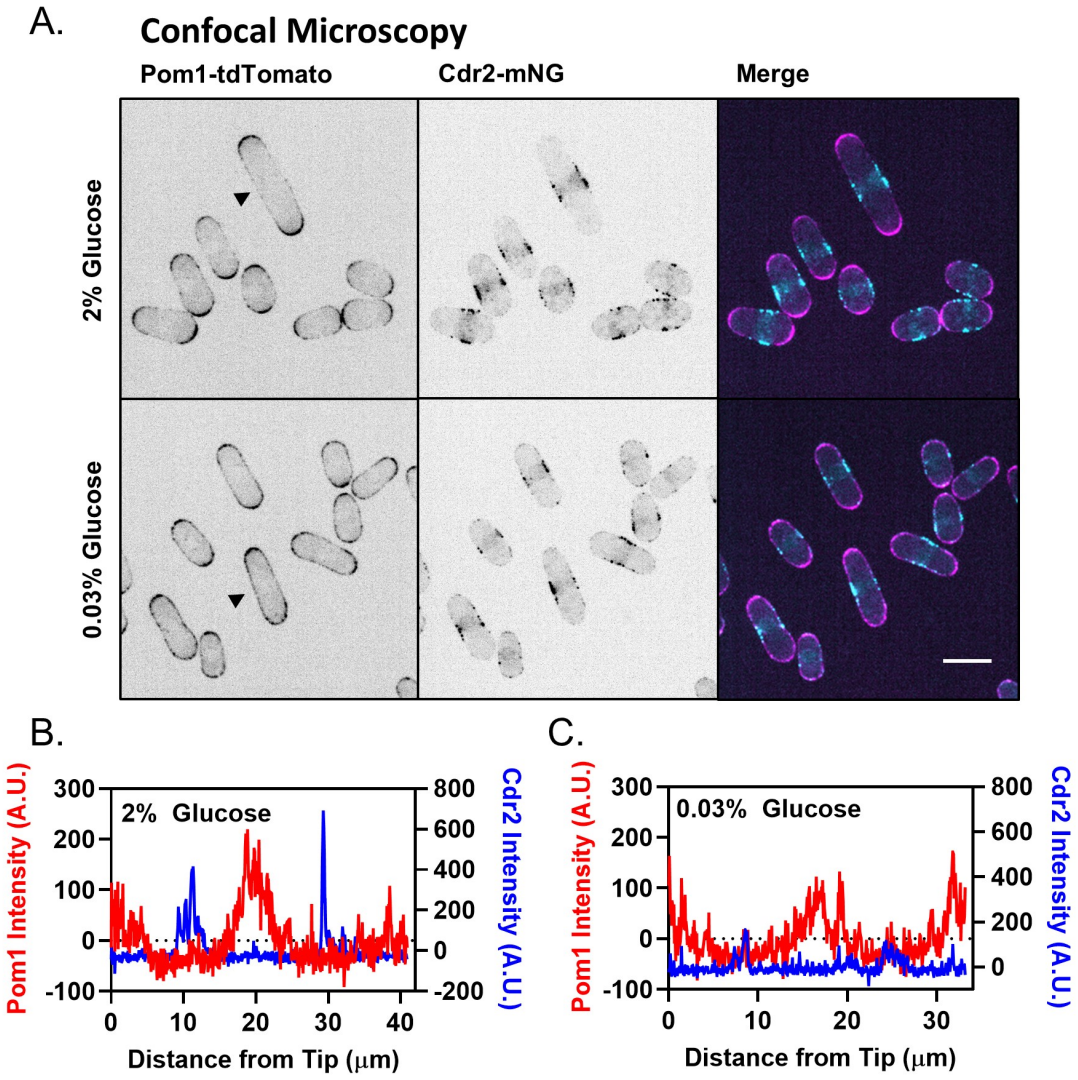

Figure 5 – figure supplement 1

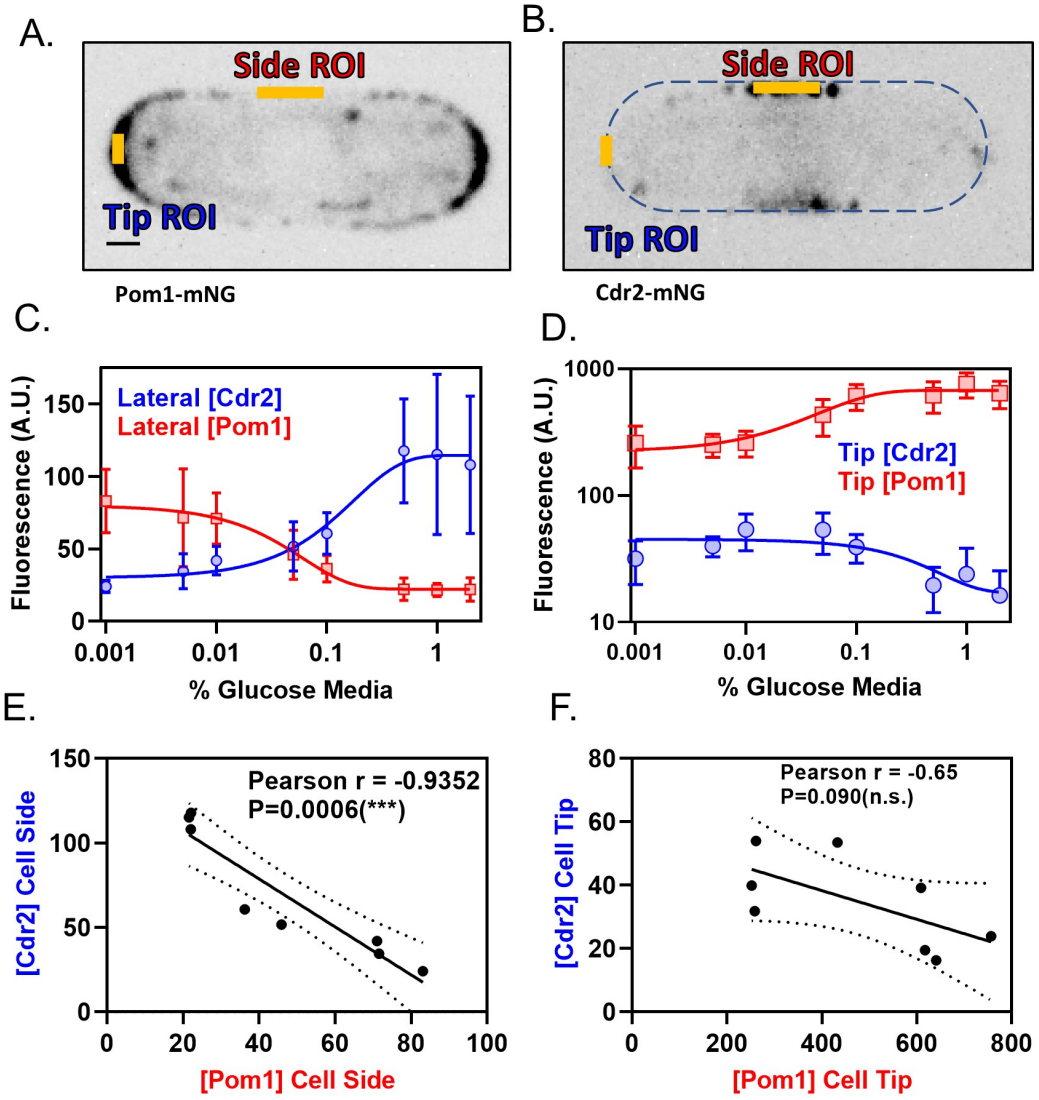
A.
Side ROI
Tip ROI
Pom1-mNG
B.
Side ROI
Tip ROI
Cdr2-mNG
C.
Lateral [Cdr2]
Lateral [Pom1]
Fluorescence (A.U.)
% Glucose Media
D.
Tip [Cdr2]
Tip [Pom1]
Fluorescence (A.U.)
% Glucose Media
E.
Pearson r = -0.9352
P=0.0006(***)
[Cdr2] Cell Side
[Pom1] Cell Side
F.
Pearson r = -0.65
P=0.090(n.s.)
[Cdr2] Cell Tip
[Pom1] Cell Tip

Figure 6

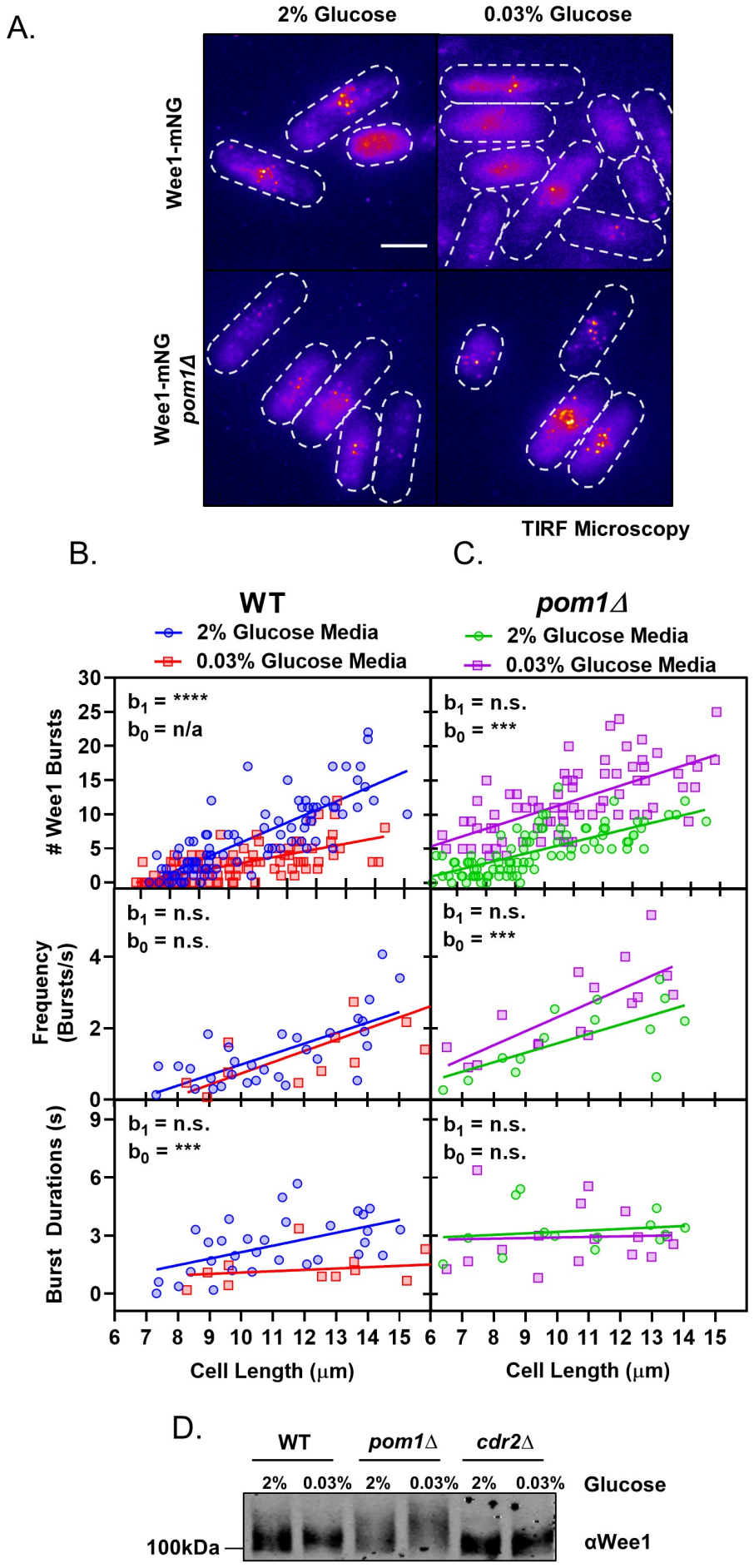
A.
2% Glucose
0.03% Glucose
Wee1-mNG
Wee1-mNG pom1Δ
TIRF Microscopy
B.
C.
WT
pom1Δ
2% Glucose Media
0.03% Glucose Media
Wee1 Bursts
Frequency (Bursts/s)
Burst Durations (s)
b1 = ****
b0 = n/a
b1 = n.s.
b0 = ***
b1 = n.s.
b0 = n.s.
Cell Length (μm)
D.
WT
pom1Δ
cdr2Δ
2% 0.03% 2% 0.03% 2% 0.03%
Glucose
100kDa
αWee1

Figure 7

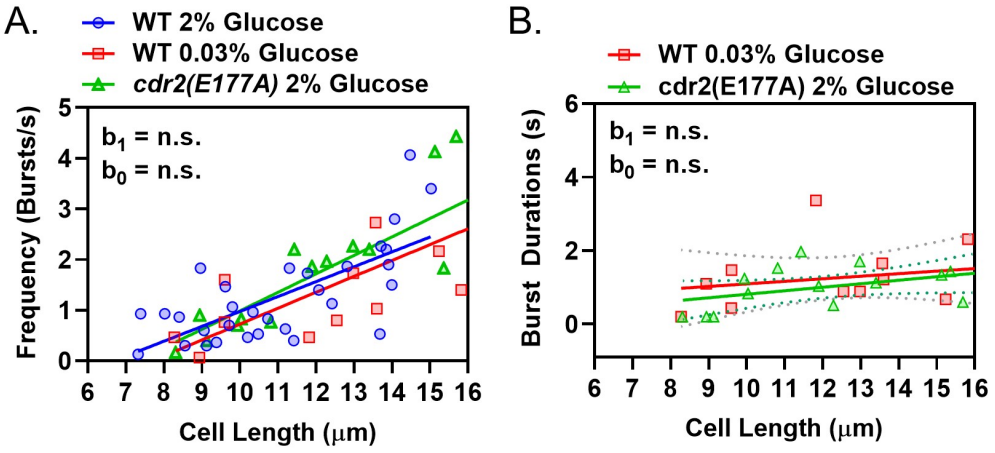

Figure 7 – figure supplement 1

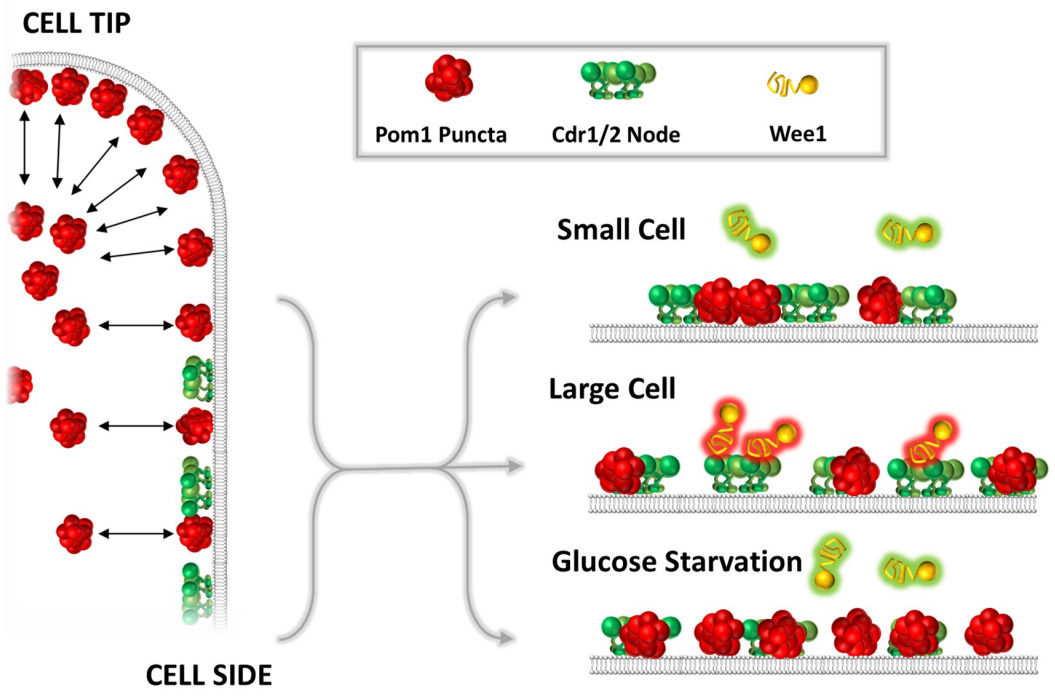
CELL TIP
Pom1 Puncta
Cdr1/2 Node
Wee1
Small Cell
Large Cell
Glucose Starvation
CELL SIDE

Figure 8